Chemical Evolution of Some Selected Complex Organic Molecules in Low-mass Star-forming Regions

The Astrophysical Journal, 958:111 (26pp), 2023 December 1 https://doi.org/10.3847/1538-4357/acfc4d

Chemical Evolution of Some Selected Complex Organic Molecules in Low-mass Star-forming Regions

Bratati Bhat[1], Rumela Kar[2], Suman Kumar Mondal[3], Rana Ghosh[4], Prasanta Gorai[5], Takashi Shimonishi[6,7], Kei E. I. Tanaka[8], Kenji Furuya[9], and Ankan Das[1]
[1] Institute of Astronomy Space and Earth Science, AE/C, 28/1, Arjunpur, Baguiati, Kolkata, 700059, India; ankan.das@gmail.com
[2] Department of Metallurgical Engineering and Material Sciences, IIT Bombay, Powai, Mumbai, Maharashtra, 400076, India
[3] S.N. Bose National Center for Basic Sciences, JD-Block, Salt Lake, Kolkata, 700098, India
[4] Indian Centre for Space Physics, 43 Chalantika, Garia Station Road, Kolkata, 700084, India
[5] Department of Space, Earth & Environment, Chalmers University of Technology, SE-412 96 Gothenburg, Sweden
[6] Center for Transdisciplinary Research, Niigata University, Nishi-ku, Niigata 950-2181, Japan
[7] Environmental Science Program, Department of Science, Faculty of Science, Niigata University, Nishi-ku, Niigata 950-2181, Japan
[8] Department of Earth and Planetary Sciences, Tokyo Institute of Technology, Meguro, Tokyo, 152-8551, Japan
[9] Center for Computational Sciences, University of Tsukuba, Tsukuba, 305-8577, Japan & National Astronomical Observatory of Japan, Tokyo 181-8588, Japan
Received 2022 August 26; revised 2023 August 16; accepted 2023 August 17; published 2023 November 16

Abstract

The destiny of complex organic molecules (COMs) in star-forming regions is interlinked with various evolutionary phases. Therefore, identifying these species in diversified environments of identical star-forming regions would help to understand their physical and chemical heritage. We identified multiple COMs utilizing the Large Program Astrochemical Surveys At Institut de Radio Astronomie Millimétrique (IRAM) data, dedicated to chemical surveys in Sun-like star-forming regions with the IRAM 30 m telescope. It was an unbiased survey in the millimeter regime, covering the prestellar core, protostar, outflow region, and protoplanetary disk phase. Here, we report the transitions of seven COMs, namely, methanol (CH_3OH), acetaldehyde (CH_3CHO), methyl formate (CH_3OCHO), ethanol (C_2H_5OH), propynal (HCCCHO), dimethyl ether (CH_3OCH_3), and methyl cyanide (CH_3CN) in sources L1544, B1-b, IRAS4A, and SVS13A. We found a trend among these species from the derived abundances using the rotational diagram method and Monte Carlo Markov chain fitting. We have found that the abundances of all of the COMs, except for HCCCHO, increase from the L1544 (prestellar core) and peaks at IRAS16293-2422 (class 0 phase). It is noticed that the abundance of these molecules correlates with the luminosity of the sources. The obtained trend is also visible from the previous interferometric observations and considering the beam dilution effect.

Unified Astronomy Thesaurus concepts: Astrochemistry (75); Star forming regions (1565); Interstellar medium (847); Interstellar molecules (849); Interstellar abundances (832)

Supporting material: figure sets, machine-readable table

1. Introduction

One of the most compelling topics of contemporary astrophysics is understanding matter's chemical origin and evolution during the formation of stars (Caselli & Ceccarelli 2012). Interstellar matter consists of molecules and dust produced during a stellar cycle. These molecules play a dominant role in gas cooling and initiate gravitational collapse, giving birth to many stars. It is thus vital to understand and characterize the evolutionary anatomy of our solar system. This study is particularly interested in the formation of low-mass stars across different evolutionary stages. It begins with the fragmentation of a molecular cloud into several gravitationally bound cores supported against gravity by thermal, magnetic, and turbulent pressures. The prestellar core has a temperature of $\leqslant$30 K (Garrod & Herbst 2006; Garrod et al. 2009). It is currently understood that many complex molecules or precursors could have been formed by the active grain catalysis process (Hasegawa et al. 1992; Das et al. 2008, 2010, 2016; Das & Chakrabarti 2011; Srivastav et al. 2022; Sil et al. 2021; Bhat et al. 2022; Ghosh et al. 2022). Unfortunately, due to the low temperature of this region, it is buried under interstellar ice, which makes it challenging to observe. However, due to the refinement of existing observation facilities, many complex organic molecules (COMs) have been identified in prestellar cores such as L1544, L183, L1512 and L1498 (Lattanzi et al. 2020; Caselli et al. 2017; Vastel et al. 2018). Once a prestellar core becomes unstable and gravitational collapse ensues, the gravitational energy freely radiates away, and the collapsing fragment remains isothermal. Initially, a robust central concentration of matter is formed due to this isothermal collapse. Hence, an opaque, hydrostatic protostellar core in the center of a thick envelope remains, wherefrom it accretes matter. In the beginning, the central object is obscured due to the thickness of the envelope. The cold outer regions of the envelope govern the spectral energy distribution. This phase is represented by the class 0 phase of star formation (Andre et al. 1993). While the major parts of the envelope are glacial, there seems to be a depletion of heavy element-bearing molecules frozen into the grain mantles, precisely as found in prestellar cores. However, the presence of the central core is fueled by gravitational energy, which causes heating of the innermost region of the envelope. This causes evaporation of the grain mantles formed during the prestellar core phase, and the

Table 1
Targeted Positions and Relevant Information of the Sample Sources

Source name	Stage of the source	Coordinates (J2000)	Distance (pc)[b]	Luminosity ($L_\odot$)[c]	V_{LSR} (km s^{-1})
L1544	Evolved prestellar core	$05^h04^m17\overset{s}{.}21+25°10'42\overset{''}{.}8$	140 (171.7)[a]	1.0	7.2 (Jiménez-Serra et al. 2016)
B1-b	FHSC	$03^h33^m20\overset{s}{.}80+31°07'34\overset{''}{.}0$	230	0.77	6.5 (López-Sepulcre et al. 2015)
IRAS4A	Class 0	$03^h29^m10\overset{s}{.}42+31°13'32\overset{''}{.}2$	260 (293)[a]	9.1	7.2 (Gerin et al. 2009)
SVS13A	Class I	$03^h29^m03\overset{s}{.}73+31°16'03\overset{''}{.}8$	260 (300)[a]	34.0	8.6 (Chen et al. 2009)

Notes.
[a] Updated distance.
[b] See Section 2.
[c] See Section 2.

molecules trapped in the ice are introduced to the gas phase, where they may undergo further reactions. Expanding over 100 au, they form a hot corino. Hot corinos share some similarities with hot cores, but they are not be considered scaled versions of each other and differ chemically (Bottinelli et al. 2007). Hot cores are rich in COMs. Many COMs are detected in high-mass star-forming regions (Gorai et al. 2020, 2021; Mondal et al. 2021, 2023). The most notable hot corinos are IRAS 16293-2422, IRAS4A IRAS4B, IRAS2A, HH212, L483, and B335 (Sahu et al. 2018; Jørgensen et al. 2004; Jaber et al. 2014; Santangelo et al. 2015; Jacobsen et al. 2019). A class 0 core starts to evolve into class I after the accretion of more than half of its envelope onto the central core. After a million years, with the onset of thermonuclear fusion in this core, a mighty stellar wind is produced, which restricts the infall of new masses. Obtained evidence suggests that the chemical composition of minor components of our solar system (comets, asteroids, etc.) is partially obtained from the early stages of solar-type protostar formation (Bockelée-Morvan et al. 2000). Class I sources would act as a bridge between class 0 and the prominent disk present in the class II and III phases of star formation. Comparatively more complex molecules ($HCOOCH_3$, CH_3OCH_3, CH_3CHO, CH_3OH, HCOOH, CH_3CH_2OH, NH_2CHO, CH_3CN, etc.) have been observed in the hot corino phase than the protoplanetary disk. Radio astronomy and far-infrared observatories play a spectacular role in modern-day astrophysics. Radio telescopes that operate in the millimeter wave bands probe the cold universe, making it possible to make detailed observations of systems at different evolutionary stages, which will ultimately shed light on the most decisive chemical processes determining evolution. One of the most important tools to comprehensively study the evolution of star-forming regions is systematic spectral line surveys, especially in the millimeter range. Recent remarkable progress in observational facilities in radio and far-infrared regimes has sparked a new molecular detection era in star-forming regions. Dedicated line surveys of different astronomical sources at diverse evolutionary stages of star formation will be beneficial in understanding the chemical evolution during the star formation stages. Here, we have analyzed the Large Program Astrochemical Surveys At Institut de Radio Astronomie Millimétrique (IRAM) 30 m data for L1544, B1-b, IRAS4A, and SVS13A to understand the chemical evolution through the different stages of low-mass star-forming regions.

This paper is organized as follows. In Section 2, we discuss the observational details. Results and discussions are presented in Section 3, and finally, in Section 4, we conclude.

2. Observations

We used the archival data of the Large Program of Astrochemical Surveys At IRAM (ASAI; principal investigators: Bertrand Lefloch and Rafael Bachiller). This systematic line survey was dedicated to understanding solar-type protostars' chemical and dynamical evolution. The observation was carried out from 2012 September to 2015 March using the extensive millimeter interferometer receivers (EMIRs) of the IRAM 30 m telescope. This work considers four different sources L1544, B1-b, IRAS4A, and SVS13A (belonging to four distinct stages from the prestellar phase to class I). The survey contained EMIR template sources at different stages of evolution. The 3 mm (80–116 GHz), 2 mm (130–170 GHz), and 1.3 mm (200–276 GHz) bands were covered by this line survey. While all these bands were covered for B1b, IRAS4A, and SVS3A, in the case of L1544, only the 3 mm (80–116 GHz) band was covered. The observational details were already discussed elaborately in Lefloch et al. (2018). The beam size or half power beamwidth (HPBW) of the IRAM 30 m telescope can be determined by the HPBW ($''$) = 2460/frequency (GHz) relation. Here, the antenna temperature (T_A^*), was converted to the main beam temperature (T_{MB}), by $T_{MB} = T_A^*/\eta_{MB}$, where η_{MB} is the antenna efficiency. All the intensities in the tables and figures are shown in terms of the main beam temperature. The details of the sources considered here are discussed in the section below. The targeted positions and necessary information about these sources are summarized in Table 1.

2.1. Sources Considered

2.1.1. L1544

In the Taurus molecular cloud (TMC), L1544 is a dense starless core that is in an early phase of star formation before collapse (Tafalla et al. 1998; Ciolek & Basu 2000). This ideal proto-type evolved prestellar core is situated at 140 pc distance from the Sun (Cernicharo & Guelin 1987). Recently, Galli et al. (2019) using Gaia data obtained a distance of 171.7 pc for L1544. The central part of the prestellar core (up to a few thousand au scale) was unexplored until Caselli et al. (2019, 2022) used the Atacama Large Millimeter/submillimeter Array (ALMA) high angular resolution band 6 continuum emission data. They named the compact region of 0.1 $M_\odot$ (10$''$ radius ∼1400 au) as the "kernel." Besides the possible local density enhancement, this kernel has an average number density of $\sim 10^6$ cm^{-3}. Although this kernel is fragmented, non-ideal magnetohydrodynamic simulations and synthetic interferometric observations suggest a smooth kernel with a peak number density of 10^7 cm^{-3}. In the prestellar core

phase, matter accumulating in the center of the cloud yielded a drop in temperature and a growth in density. As a result, the atoms and molecules in the gas phase froze on the dust and formed icy grain mantles. A central density of $\sim 10^6$ cm^{-3} was reached along with a very low temperature $\sim$7 K. Due to heavy depletion, a high degree of deuterium fractionation of N_2H^+ compared to HCO^+ is observed (Caselli et al. 2002; Redaelli et al. 2019). Many COMs are detected in L1544 (Vastel et al. 2014), ranging from numerous sulfur-related molecules to prebiotic molecules (Vastel et al. 2018; López-Sepulcre et al. 2015). Detailed modeling of L1544 by Keto & Caselli (2010) found that they needed to consider a high dust opacity to reproduce the measured temperature drop within 2000 au. Caselli et al. (1999) indicated that it could mean fluffy grains in the core center, where CO is heavily frozen, and volume densities become greater than 10^6 cm^{-3}. Numerous observations well constrain the physical structure of this source. The high volume densities and centrally concentrated form make it a unique target to study possible variations in opacity.

2.1.2. B1-b

Barnard 1 (B1) belongs to the Perseus molecular cloud complex situated at a distance of 230 pc (Fuente et al. 2017). It is an important source from chemical and kinematic points of view because it contains several active sources that are in different stages of star formation. For example, B1-a and B1-c are in the class 0 stage, associated with outflows. B1-b is the main core divided into three parts: two young stellar objects, B1b-N and B1b-S, and one more evolved entity, B1b-W (Huang & Hirano 2013; Fuente et al. 2016). B1b-N and B1b-S are separated from each other by approximately 18″, which are in the first hydrostatic core (FHSC) stage. The FHSC is categorized based on the spectral energy distribution and outflow present within it (Gerin et al. 2015; Pezzuto et al. 2012). The most investigated part is B1-b because of its rich molecular spectrum. The total luminosity of source B1-b is 0.77 $L_\odot$ (Lefloch et al. 2018). Numerous species, such as CH_3O (Cernicharo et al. 2012), NH_3D^+ (Cernicharo et al. 2013), and HCNO (Marcelino et al. 2009), were identified in this source. The detection of D_2CS, ND_2H, and ND_3 confirms the high deuteration observed toward this source. Recent observation using the ALMA interferometer have identified various COMs, such as CH_3OCOH, CH_3CHO, and many COMs (NH_2CN, NH_2CHO, CH_3CH_2OH, CH_2OHCHO, CH_3CH_2OCOH) is tentatively detected toward B1-b (Marcelino et al. 2018b).

2.1.3. NGC 1333-IRAS4A

IRAS4A is a proto-binary system located in the NGC 1333 reflection nebula in the Perseus cloud. The recent result from Gaia found that it is situated at a distance of $\sim 293 \pm 22$ pc (Ortiz-León et al. 2018; Zucker et al. 2018). The total mass of the gas envelope of IRAS4A is 3.5 $M_\odot$, and the total luminosity is 9.1 $L_\odot$ (Lefloch et al. 2018). Another component, IRAS4B, is separated by an angular distance of 31″ from IRAS4A (Marvel et al. 2008). To date, many COMs like CH_3OH, CH_3OCH_3, C_2H_5CN, and CH_2OHCHO are detected toward IRAS4A. It is noticed that a very high collimated outflow is associated with IRAS4A from CO, CS, and SiO emission (Blake et al. 1995; Lefloch et al. 1998). The infall motion was detected in this source by Di Francesco et al. (2001) and Choi et al. (1999) with an estimated accretion rate of 1.1×10^{-4} $M_\odot$ per year, an inner mass of 0.7 $M_\odot$, and age of $\sim$6500 yr (see also Maret et al. 2002). Previous observations with the IRAM 30 m classify IRAS4A as a hot corino protostar. Recently, high-resolution interferometric data revealed that IRAS4A consists of two components (Choi et al. 2010, 2011), namely IRAS4A1, and IRAS4A2, separated by an angular distance of 1.8″ ($\sim$527 au; De Simone et al. 2020) from one another. A striking chemical difference is observed between IRAS4A1 and IRAS4A2. Santangelo et al. (2015) and López-Sepulcre et al. (2017) confirmed that IRAS4A2 is a hot corino protostar, but more analysis is needed to confirm it for IRAS4A1. Recently De Simone et al. (2020) concluded that IRAS4A1 is a hot corino, but the lack of interstellar complex organic molecules (iCOMS) detected toward IRAS4A1 is due to a large dust optical depth toward the center. Sahu et al. (2019) depicted two possible scenarios of IRAS4A1: (a) the observed absorption features probably arise from a hot-corino-like atmosphere against a very compact ($\leqslant$36 au) disk in A1; (b) the absorption may arise from different layers of a temperature-stratified dense envelope in A1.

2.1.4. SVS13A

SVS13A is a relatively evolved protostar already in the class I phase. The luminosity of the source is 34 $L_\odot$ and located at a distance of $\sim$260 pc (Schlafly et al. 2014). Recently, using Gaia data, the distance of SVS13A is 300 PC (Diaz-Rodriguez et al. 2022). It is a part of the NGC 1333-SVS13 system. It consists of three sources, A, B, and C. The angular separation of SVS13A from its two counterparts, SVS13B and SVS13C, are 15″ and 20″, respectively (Bachiller et al. 1998; Looney et al. 2007). SVS13A has an extended outflow associated with it, also attached to well-known Herbig–Haro chain (HH) objects 7–11 (Reipurth et al. 1993). The VLA observation revealed SVS13A as a closed binary system, VLA4A and VLA4B, separated by 0.3″ ($\sim$70 au; Anglada et al. 2000). A recent observation by Diaz-Rodriguez et al. (2022) reported a distance of $\sim$300 pc for SVS13A and separation of VLA4A and VLA4B of $\sim$90 au. Many COMs, such as acetaldehyde (CH_3CHO), methyl formate ($HCOOCH_3$), dimethyl ether (CH_3OCH_3), ethanol (CH_3CH_2OH), and formamide (NH_2CHO) were already identified from the ASAI data in this source (Bianchi et al. 2019).

2.2. Line Identification

The line identification is carried out using CASSIS[10] software. For the spectroscopic details, we have used the Cologne Database for Molecular Spectroscopy[11] (Müller et al. 2001, 2005) and Jet Propulsion Laboratory (JPL)[12] (Pickett et al. 1998) databases. We only consider unblended lines with a signal-to-noise ratio greater than the 3σ limit. The observed transitions of various complex molecules together with their quantum numbers, upper-state energies (E_{up}), V_{LSR}, line parameters such as line width (full width at half maximum, FWHM), and the integrated intensity ($\int T_{mb} dV$) are noted in Table A1. The line parameters are obtained using a single Gaussian fit to the observed spectral profile of each unblended

[10] http://cassis.irap.omp.eu/?page=cassis
[11] https://cdms.astro.uni-koeln.de/
[12] https://spec.jpl.nasa.gov/

transition. The identified lines are plotted in black color in Figure D1 and the online figure set.

2.3. H_2 Column Density

Due to the lack of continuum observation data, we used the H_2 column density from the literature to derive the abundances of species. For L1544, we used a H_2 column density of 8.9×10^{22} cm^{-2} (calculated by Hily-Blant et al. 2022) for a beam size of 26″ in L1544. Daniel et al. (2013) obtained an average H_2 column density (1.2 mm observation with IRAM) of 7.6×10^{22} cm^{-2} within the 30″ beam in B1. Johnstone et al. (2010) estimated a H_2 column density $\sim 8.2 \times 10^{22}$ cm^{-2} for the same beam. Following López-Sepulcre et al. (2015), we used an average H_2 column density $\sim 7.9 \times 10^{22}$ cm^{-2} for B1-b in estimating the abundances. For IRAS4A, Maret et al. (2002) obtained a H_2 column density of 2.9×10^{22} cm^{-2} for a 30″ beam, whereas with a 0.5″ beam it was 2.5×10^{24} cm^{-2}. Since we analyzed the data obtained from the IRAM 30 m telescope, we use 2.9×10^{22} cm^{-2} for abundance estimation. For SVS13A, we used the H_2 column density of 10^{23} cm^{-2} estimated by Lefloch et al. (1998) for a 20″ beam. Due to this uncertainty in the H_2 column density, the derived abundances and the chemical trend also have an uncertainty. To minimize this effect, we used the values of H_2 column density in different sources for the ∼30″ beam. The H_2 column density used in deriving the abundances is summarized in Table C1.

3. Results and Discussions

The main goal of this work is to find the correlation between the observed COMs in various evolutionary phases of star-forming regions. Observing all the instances of a single low-mass star-forming region is impossible. Instead, it is beneficial to selectively follow some evolutionary stages of similar types of the ongoing process before the formation of stars to have an overview of the complete process. Although it is not expected that all the targeted regions will follow a similar path, it gives an overall idea of the general low-mass star formation process. We were able to identify several transitions of interstellar COMs, i.e., methanol (CH_3OH), acetaldehyde (CH_3CHO), methyl formate (CH_3OCHO), ethanol (C_2H_5OH), propynal (HCCCHO), dimethyl ether (CH_3OCH_3), and methyl cyanide (CH_3CN), in different sources.

We apply two robust LTE methods, namely rotational diagram (RD) analysis and Monte Carlo Markov chain (MCMC) fitting, to derive the column density and excitation temperature of a species. The details of the RD analysis and MCMC method are discussed in Sections C and D, respectively. The obtained column densities and temperature from RD analysis are summarized in Table C1. The rotation diagram plots are shown in Figure C1 and its online-only figure set. The variable parameters and the ranges used for the MCMC method and the best fitted values are summarized in Table D1. In addition, Table 2 compares the abundances obtained through MCMC fitting and RD analysis with earlier findings. It depicts that our results are consistent with the earlier results. The values obtained using both methods differ from the previously obtained values within a factor of 0.17–5.02. Also, the abundances obtained from RD analysis and MCMC fitting are almost similar and differ within a minimal range, which justifies the accuracy of the results obtained from the two methods. In the left panel of Figure 1, we show how the abundances obtained from the RD method vary in different sources, whereas the right panel shows similar results obtained with the MCMC fitting method. The results obtained from our analysis are discussed here with individual species. The column density values of H_2 in different sources are from the literature to calculate the abundances. The values are noted in Table C1 and in Section 2.3.

3.1. Observed Species

3.1.1. CH_3OH

Since methanol is a major chemical constituent of the various phases of star formation, its analysis has become of utmost importance. Previously, Vastel et al. (2014) identified CH_3OH emission in L1544 from the ASAI data and obtained a column density 3×10^{13} cm^{-2} using non-LTE approximation. They concluded that methanol lines likely originated from ∼8000 au, where the temperature is ∼10 K. Methanol was previously detected in B1-b using the IRAM 30 m telescope by Öberg et al. (2009) with a column density of 2.5×10^{14} cm^{-2}. In IRAS4A, Maret et al. (2005) obtained a column density of 5.1×10^{14} cm^{-2}. Here, we have identified several transitions of CH_3OH in all four sample sources (see Table A1). The obtained values of column densities and excitation temperatures noted from the RD method are presented in Table C1 and the same for MCMC fitting is noted in Table D1. We have performed MCMC fitting considering a single component of the detected CH_3OH transitions in L1544, B1-b, and SVS13A, and we get a good fit. In the case of class 0 protostar IRAS4A, we found that a two-component fit is required for the RD of methanol: (1) having $E_{up} > 50$ K (hot component), (2) having $E_{up} < 50$ K (cold component). Similarly, in the MCMC method, we obtain a good fit when we consider two components. The chemical evolution of CH_3OH with respect to the evolutionary stages of star formation is represented by red bars in the left (RD) and right (MCMC) panels of Figure 1. It shows that the methanol abundance gradually increases from a minimum value in L1544 to a maximum value in IRAS16293-2422. The increase in abundance might be attributed to the gradual rise in temperature. Since a lower temperature (10–20 K) is efficient for the ice phase hydrogenation reactions, methanol formation by successive hydrogen additions to CO could be possible during the prestellar core phase.

$$CO \rightarrow HCO \rightarrow H_2CO \rightarrow CH_2OH/CH_3O \rightarrow CH_3OH$$

However, at this stage, the thermal desorption is not efficient enough (Das et al. 2018, having a binding energy of 5264 K) to transfer the ice phase methanol contents to the gas phase. The non-thermal desorptions (Öberg et al. 2009; Garrod et al. 2007) are mainly responsible for the observed gas-phase abundance of methanol at this stage. Furthermore, the cloud evolves into an FHSC and then a protostar phase. In the protostar phase, methanol would also be formed by a radical–radical surface reaction, $CH_3 + OH \rightarrow CH_3OH$. As a result, the temperature increases, eventually enhancing the chance of production and their release by thermal desorption. We get a lower abundance of methanol in SVS13A (class I object). A decrease in the abundance of methanol for the class I object may occur due to the lower methanol formation rate in the class I phase than in the class 0 phase because of the competition between the reaction and thermal desorption of the reactants.

Table 2
Comparison of Column Densities Obtained Using the RD Method and MCMC Fitting with the Values Obtained from the Literature for COMs Observed in Different Sources

Species	Column Density	L1544	B1-b	IRAS4A	SVS13A
CH_3OH	Previous	$(2.70 \pm 0.60) \times 10^{13}$[a]	$(2.50 \pm 1.30) \times 10^{14}$[b]	$(5.10 \pm 1.00) \times 10^{14}$[c]	$(1.00 \pm 0.20) \times 10^{17}$[d]
	RD	$(7.14^{+0.70}_{-0.60}) \times 10^{12}$	$(9.73^{+0.05}_{-0.04}) \times 10^{13}$	$(1.42^{+0.03}_{-0.02}) \times 10^{14}$ $(1.41^{+0.04}_{-0.04}) \times 10^{14}$	$(1.21^{+0.03}_{-0.02}) \times 10^{14}$
	MCMC	$(4.60 \pm 0.92) \times 10^{12}$	$(1.13 \pm 0.16) \times 10^{14}$	$(1.80 \pm 0.29) \times 10^{14}$(C1) $(2.00 \pm 0.28) \times 10^{14}$(C2)	$(2.43 \pm 1.07) \times 10^{14}$
CH_3CHO	Previous	1.20×10^{12}[h]	1.50×10^{12}[f]	2.60×10^{12}[g]	$(1.20 \pm 0.70) \times 10^{16}$[d]
	RD	$(1.25^{+0.40}_{-0.30}) \times 10^{12}$	$(3.48^{+0.5}_{-0.50}) \times 10^{12}$	$(9.47^{+0.6}_{-0.50}) \times 10^{12}$ $(9.53^{+1.00}_{-0.90}) \times 10^{12}$	$(5.89^{+1.6}_{-1.30}) \times 10^{12}$
	MCMC	$(6.10 \pm 3.55) \times 10^{11}$	$(4.40 \pm 0.56) \times 10^{12}$	$(1.30 \pm 0.21) \times 10^{13}$(C1) $(1.10 \pm 0.21) \times 10^{13}$(C2)	$(7.20 \pm 4.89) \times 10^{12}$
CH_3OCHO	Previous	$(4.40 \pm 4.00) \times 10^{12}$[h]	3.00×10^{12}[f] (A+E)	$(5.50 \pm 2.70) \times 10^{16}$[i](A) $(5.80 \pm 1.10) \times 10^{16}$[i](E)	$(1.30 \pm 0.10) \times 10^{17}$[d]
	RD	3.70×10^{12}[x]	$(6.41^{+2.30}_{-5.00}) \times 10^{12}$	$(3.49^{+0.50}_{-0.40}) \times 10^{13}$	$(7.78^{+1.30}_{-1.00}) \times 10^{13}$
	MCMC	⋯	$(1.20 \pm 1.57) \times 10^{13}$	$(3.65 \pm 1.63) \times 10^{13}$	$(7.10 \pm 3.52) \times 10^{13}$
C_2H_5OH	Previous		$\leqslant 4.80 \times 10^{12}$[j]	$(4.40 \pm 1.40) \times 10^{16}$[k]	$(1.10 \pm 0.50) \times 10^{17}$[d]
	RD	⋯	1.00×10^{13}[x]	$(1.69^{+0.30}_{-0.20}) \times 10^{13}$	$(1.37^{+1.80}_{-1.60}) \times 10^{13}$
	MCMC	⋯	-	$(2.10 \pm 1.10) \times 10^{13}$	$(1.60 \pm 1.22) \times 10^{13}$
HCCCHO	Previous	$1.80 - 6.30 \times 10^{11}$[h]	5.50×10^{11}[f]	⋯	$\leqslant 1.00 \times 10^{16}$[d]
	RD	$(3.16^{+0.80}_{-0.70}) \times 10^{12}$	2.56×10^{12}[x]	3.90×10^{12}[x]	4.00×10^{14}[x]
	MCMC	$(4.00 \pm 1.33) \times 10^{11}$	⋯	⋯	-
CH_3OCH_3	Previous	$(1.50 \pm 0.20) \times 10^{12}$[h]	3.00×10^{12}[f]	$\leqslant 4.50 \times 10^{16}$[i]	$(1.40 \pm 0.40) \times 10^{17}$[d]
	RD	1.72×10^{12}[y]	6.12×10^{12}[y]	$1.20^{+0.40}_{-0.30} \times 10^{13}$	1.41×10^{13}[y]
	MCMC	$(2.20 \pm 1.61) \times 10^{12}$	$(8.50 \pm 5.52) \times 10^{12}$	$(2.10 \pm 1.03) \times 10^{13}$	
CH_3CN	Previous	$(6.1 \pm 1.8) \times 10^{11}$[l]	$(3.2^{+1.6}_{-1.4}) \times 10^{14}$[v](B1- b S) $<8.5 \times 10^{13}$[v] (B1-b N)	$(6.5 \pm 2.9) \times 10^{15}$[m]	2.0×10^{16}[n]
	RD	4.85×10^{11}[y]	4.95×10^{11}[y]	$(1.78^{+0.17}_{-0.15}) \times 10^{12}$	$(4.57^{+0.23}_{-0.22}) \times 10^{12}$
	MCMC	⋯	⋯	$(1.34 \pm 0.35) \times 10^{12}$	$(2.8 \pm 0.57) \times 10^{12}$

Notes.
[x] Upper limits,
[y] LTE fitting.
[a] Bizzocchi et al. (2014),
[b] Öberg et al. (2009),
[c] Maret et al. (2005),
[d] Bianchi et al. (2019; interferometric observation),
[f] Cernicharo et al. (2012),
[g] Holdship et al. (2019),
[h] Jiménez-Serra et al. (2016),
[i] Bottinelli et al. (2004; interferometric observation),
[j] Öberg et al. (2010),
[k] Taquet et al. (2015; interferometric observation),
[l] Nagy et al. (2019),
[m] Taquet et al. (2015; interferometric observation),
[n] Bianchi et al. (2022b; interferometric observation),
[v] Yang et al. (2021; interferometric observation).

Scibelli & Shirley (2020) surveyed the presence of COMs in starless and prestellar cores within the TMC using ARO 12 m telescope on Kitt Peak (beam size ∼62.3″). They obtained a methanol abundance (0.53–3.36) × 10^{-9}, and excitation temperatures ranging from 6.79 to 8.66 K for all 31 cores. From the RD analysis, we obtained a comparatively lower abundance of methanol ∼8.02 × 10^{-11}, in L1544 and an excitation temperature of 8.6 K. Scibelli & Shirley (2020) found that the less evolved regions have comparatively higher methanol abundance than more evolved regions. Since L1544 is more evolved than the sources studied by Scibelli & Shirley (2020), a comparatively lower abundance of methanol is consistent with the observed trend.

3.1.2. CH_3CHO

Acetaldehyde is an asymmetric top molecule with a widespread presence in the various evolutionary phases of star formation. We have identified multiple transitions of CH_3CHO in all the selected sources. Fitted line parameters of this species are summarized in Table A1. The upper-state energy of the observed lines ranges from 9 to 121 K. Jiménez-Serra et al. (2016) obtained a column density 1.2 × 10^{12} cm^{-2} toward the

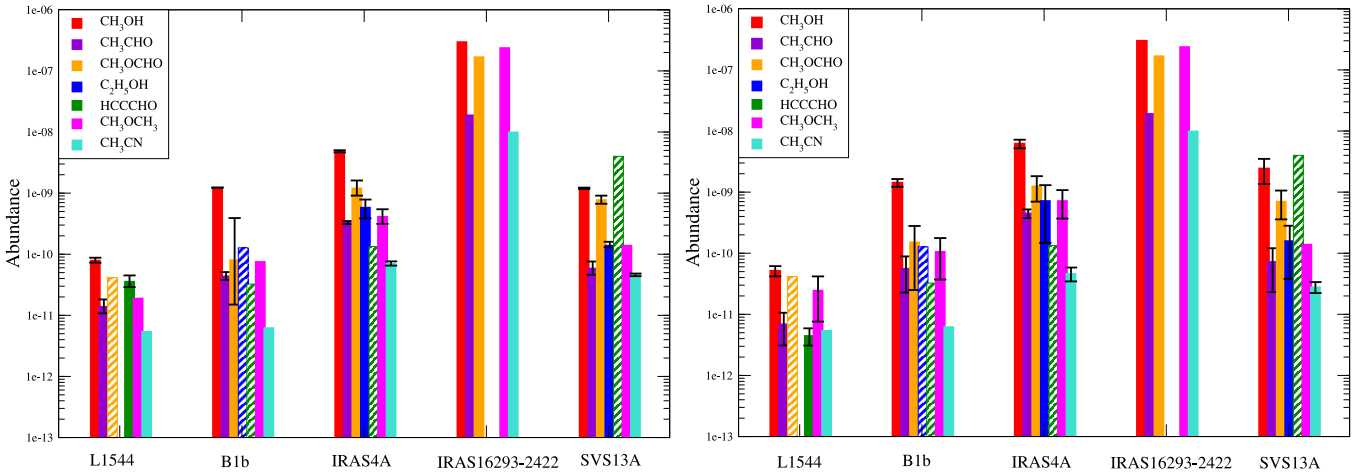

Figure 1. The evolution of abundances in different stages of low-mass star-forming regions. The left panel shows the abundances obtained from the RD method (dashed parts are the upper limits), and the right panel depicts the same obtained with the MCMC fitting. Black vertical lines represent the error bars. For CH_3OCH_3 in L1544 and B1b, the lines have the same upstate energy, so a rotation diagram cannot be performed, and the column density is calculated using simple LTE fitting. For CH_3OCH_3 in SVS13A, the column density is calculated using the value from Bianchi et al. (2019) scaling it for a 30″ beam. A new class 0 source, IRAS16293-2422 (22 $L_\odot$), is included where CH_3OH, CH_3CHO, CH_3OCHO, CH_3OCH_3, and CH_3CN are observed (Cazaux et al. 2003).

dense, highly extinguished continuum peak within the inner 2700 au and 3.2×10^{12} cm^{-2} toward a low-density shell located at 4000 au from the core center. However, we obtain a very similar column density of 1.25×10^{12} cm^{-2} for acetaldehyde in our work. In B1-b, a column density of 1.5×10^{12} cm^{-2} was obtained by Cernicharo et al. (2012) with the MADEX code assuming the excitation temperature of 10 K. From our RD analysis, we found a column density 3.5×10^{12} cm^{-2} for this species. Holdship et al. (2019) and Bianchi et al. (2019) observed CH_3CHO toward IRAS4A and SVS13A and obtained a column density of 2.6×10^{12} cm^{-2} and 1.2×10^{16} cm^{-2}, respectively, using single-dish telescope. From our RD analysis, we yielded the column densities of 9.5×10^{12} cm^{-2} and 5.9×10^{12} cm^{-2} for IRAS4A and SVS13A, respectively. Similar to the CH_3OH, for CH_3CHO, two components are observed in the RD analysis (see the online version of Figure C1) in IRAS4A, (1) $E_{up} > 50$ K (hot component) and (2) cold component having $E_{up} < 50$ K. We obtain a temperature of 22.1 K for the low excitation lines and 64.5 K for the high excitation lines from RD analysis. Similarly, a two-component MCMC fit is performed and yields a temperature of 71.2 and 11.1 K for components 1 and 2, respectively. It is noticed that the results derived from the two methods are very similar. The violet-colored bar lines in Figure 1 represent the variation of its abundance and it shows the same behavior as CH_3OH throughout the evolutionary stages of star formation. Scibelli & Shirley (2020) obtained acetaldehyde abundance $(0.6–3.9) \times 10^{-10}$, and excitation temperature 3.57 K. From the RD analysis, we obtained a comparatively lower abundance of acetaldehyde $\sim 1.4 \times 10^{-11}$ in L1544 and an excitation temperature of 6 K. Similar to CH_3OH, because L1544 is more evolved than the sources studied by Scibelli & Shirley (2020), a comparatively lower abundance of acetaldehyde is consistent with the observed trend.

3.1.3. CH_3OCHO

Methyl formate is a simple asymmetric top complex organic species observed in most star-forming regions. Its isomers, acetic acid (CH_3COOH) and glycolaldehyde ($HCOCH_2OH$), are comparatively less abundant. Observing complex molecules in a prestellar core is always challenging because of their low temperature. Jiménez-Serra et al. (2016) identified methyl formate in L1544 with the IRAM 30 m telescope at two positions: one at the center of the core and another in the same place where the peak abundance of methanol arises. They found a column density values of $(4.4 \pm 4.0) \times 10^{12}$ cm^{-2} and $(2.3 \pm 1.4) \times 10^{12}$ cm^{-2} at these two positions, respectively. Cernicharo et al. (2012) observed this species toward B1-b, and derived a total column density of 3×10^{12} cm^{-2}. Bottinelli et al. (2004) observed CH_3OCHO toward the low-mass protostar IRAS4A and derived column densities of 5.5×10^{16} cm^{-2} and 5.8×10^{16} cm^{-2} for A-CH_3OCHO and E-CH_3OCHO, respectively. Bianchi et al. (2019) identified CH_3OCHO transitions toward SVS13A, and obtained a column density of 1.3×10^{17} cm^{-2}. In prestellar core L1544, one transition at 90.22765 GHz is tentatively detected. An upper limit of column density 3.7×10^{12} cm^{-2} is estimated using the LTE method (see Table B1). For B1-b, IRAS4A, and SVS13A, many transitions are detected, and the results from RD analysis and the MCMC method are shown in Table C1 and D1, respectively. The RD plot for CH_3OCHO is shown in Figure C1 (online) and the MCMC fitting is shown in Figure D1 (online figure set).

We have found that CH_3OCHO follows a similar pattern as methanol and acetaldehyde in its evolution from the prestellar core phase to the class I stage, as represented by an orange-colored bar line in Figure 1. Unlike methanol and acetaldehyde, no ice phase hydrogenation reactions are directly involved in forming CH_3OCHO. Instead, it is the radical–radical reaction between CH_3O and HCO that can form ice phase CH_3OCHO:

$$CH_3O + HCO \rightarrow CH_3OCHO.$$

The activities are restricted at low temperatures due to the high binding energy of these radicals, i.e., 4400 K for CH_3O (Wakelam et al. 2017) and 2206 K for HCO (Das et al. 2018). However, it plays an active role in the warmer region. Moreover, the binding energy of CH_3OCHO (6295 K, https://kida.astrochem-tools.org) is comparatively higher than that of methanol and acetaldehyde (Das et al. 2018, 5264 and 4573, respectively). The decline in the CH_3OCHO abundance

Table 3
Calculation of Kinetic Temperature Using Line Ratio of Observed CH_3CN Transitions

Source	Frequency (GHz)	Quantum No.	E_{up} (K)	$\int T_{mb} dv$ (K km^{-1} s^{-1})	S_{ij}	R	T_k (K)	Average T_k (K)	
L1544	91.985314	5_1–4_1	20.4	0.05	6.61439	$\frac{5_0-4_0}{5_1-4_1}$	5.12	5.12	
	91.987087	5_0–4_0	13.2	0.068	2.2051				
B1-b	91.985314	5_1–4_1	20.4	0.034	6.61439	$\frac{5_0-4_0}{5_1-4_1}$	4.41	4.41	
	91.987087	5_0–4_0	13.2	0.058	2.2051				
IRAS4A	128.75703	7_3–6_3	89	0.089	15.74921	$\frac{7_2-6_2}{7_3-6_3}$	33.79		
	128.769436	7_2–6_2	53.3	0.144	8.85861				
	128.769436	7_2–6_2	53.3	0.144	8.85861	$\frac{7_1-6_1}{7_2-6_2}$	46.24		
	128.776881	7_1–6_1	31.9	0.244	9.44898				
	128.75703	7_3–6_3	89	0.089	15.74921	$\frac{7_1-6_1}{7_3-6_3}$	37.58		
	128.776881	7_1–6_1	31.9	0.244	9.44898				
	128.75703	7_3–6_3	89	0.089	15.74921	$\frac{7_0-6_0}{7_3-6_3}$	23.19		
	128.779363	7_0–6_0	24.7	0.285	3.1501				
	128.769436	7_2–6_2	53.3	0.144	8.85861	$\frac{7_0-6_0}{7_2-6_2}$	16.66		
	128.779363	7_0–6_0	24.7	0.285	3.1501				
	147.163244	8_2–7_2	60.4	0.098	10.33654	$\frac{8_1-7_1}{8_2-7_2}$	26.44	48.60	$E_{up} >$ 50 K
	147.171751	8_1–7_1	38.9	0.232	10.85164				
	147.163244	8_2–7_2	60.4	0.098	10.33654	$\frac{8_0-7_0}{8_2-7_2}$	14.17		
	147.174588	8_0–7_0	31.8	0.258	3.61771				
	165.540377	9_3–8_3	104	0.131	22.05132	$\frac{9_2-8_2}{9_3-8_3}$	106.31		
	165.556321	9_2–8_2	68.3	0.098	11.7908				
	165.556321	9_2–8_2	68.3	0.098	11.7908	$\frac{9_1-8_1}{9_2-8_2}$	28.45		
	165.565891	9_1–8_1	46.9	0.216	12.25078				
	165.540377	9_3–8_3	104	0.131	22.05132	$\frac{9_1-8_1}{9_3-8_3}$	52.49		
	165.565891	9_1–8_1	46.9	0.216	12.25078				
	165.540377	9_3–8_3	104	0.131	22.05132	$\frac{9_0-8_0}{9_3-8_3}$	29.16		
	165.569081	9_0–8_0	39.7	0.22	4.08322				
	165.556321	9_2–8_2	68.3	0.098	11.7908	$\frac{9_0-8_0}{9_2-8_2}$	15.30		
	165.569081	9_0–8_0	39.7	0.22	4.08322				
	73.588799	4_1–3_1	16	0.127	5.16717	$\frac{4_0-3_0}{4_1-3_1}$	5.20		
	73.590218	4_0–3_0	8.8	0.169	1.72263				
	91.979994	5_2–4_2	41.8	0.082	5.78723	$\frac{5_1-4_1}{5_2-4_2}$	33.07		
	91.985314	5_1–4_1	20.4	0.179	6.61439				
	91.985314	5_1–4_1	20.4	0.179	6.61439	$\frac{5_0-4_0}{5_1-4_1}$	5.50		
	91.987087	5_0–4_0	13.2	0.221	2.2051				
	91.979994	5_2–4_2	41.8	0.082	5.78723	$\frac{5_0-4_0}{5_2-4_2}$	14.62		
	91.987087	5_0–4_0	13.2	0.221	2.2051				
	110.381372	6_1–5_1	25.7	0.233	8.03828	$\frac{6_0-5_0}{6_1-5_1}$	5.99	10.31	$E_{up} <$ 50 K
	110.383499	6_0–5_0	18.5	0.258	2.6798				
	128.776881	7_1–6_1	31.9	0.244	9.44898	$\frac{7_0-6_0}{7_1-6_1}$	5.74		
	128.779363	7_0–6_0	24.7	0.285	3.1501				
	147.171751	8_1–7_1	38.9	0.232	10.85164	$\frac{8_0-7_0}{8_1-7_1}$	5.89		
	147.174588	8_0–7_0	31.8	0.258	3.61771				
	165.565891	9_1–8_1	46.9	0.216	12.25078	$\frac{9_0-8_0}{9_1-8_1}$	6.45		

Table 3
(Continued)

Source	Frequency (GHz)	Quantum No.	E_{up} (K)	$\int T_{mb} dv$ (K km^{-1} s^{-1})	S_{ij}	R	T_k (K)	Average T_k (K)	
	165.569081	9_0–8_0	39.7	0.22	4.08322				
SVS13A	110.364353	6_3–5_3	82.8	0.08	12.40333	$\frac{6_2-5_2}{6_3-5_3}$	42.87		
	110.374989	6_2–5_2	47.1	0.109	7.34927				
	110.364353	6_3–5_3	82.8	0.08	12.40333	$\frac{6_1-5_1}{6_3-5_3}$	72.47		
	110.381372	6_1–5_1	25.7	0.114	8.03828				
	110.364353	6_3–5_3	82.8	0.08	12.40333	$\frac{6_0-5_0}{6_3-5_3}$	38.21		
	110.383499	6_0–5_0	18.5	0.093	2.6798				
	220.709016	12_3–11_3	133.2	0.265	31.00599	$\frac{12_2-11_2}{12_3-11_3}$	47.07		
	220.73026	12_2–11_2	97.4	0.294	16.07897				
	220.74301	12_1–11_1	76	0.278	16.4203	$\frac{12_0-11_0}{12_1-11_1}$	24.76	63.90	$E_{up} > 50$ K
	220.747261	12_0–11_0	68.9	0.373	16.53946				
	220.709016	12_3–11_3	133.2	0.265	31.00599	$\frac{12_1-11_1}{12_3-11_3}$	83.68		
	220.74301	12_1–11_1	76	0.278	16.4203				
	220.709016	12_3–11_3	133.2	0.265	31.00599	$\frac{12_0-11_0}{12_3-11_3}$	66.27		
	220.747261	12_0–11_0	68.9	0.373	16.53946				
	220.73026	12_2–11_2	97.4	0.294	16.07897	$\frac{12_0-11_0}{12_2-11_2}$	135.87		
	220.747261	12_0–11_0	68.9	0.373	16.53946				

at the class I stage would be attributed to the favorable sublimation rate over the reaction rate of radicals and its subsequent gas phase destruction after desorption.

3.1.4. C_2H_5OH

Ethanol (C_2H_5OH) emission was detected for the first time in 1975 toward Sagittarius B2. It was observed with the help of one of the pioneering radio telescopes of the twentieth century, the 11 m radio telescope of the National Radio Astronomy Observatory (NRAO, Zuckerman et al. (1975)). It has been observed toward low and high mass in both star-forming regions. Due to the orientation of the OH group, ethanol consists of two different conformers, one is anti and another one is gauche. A gauche$^+$ and gauche$^-$ state forms when the tunneling between the two equivalent gauche conformers lifts the degeneracy. Recently, Bianchi et al. (2019) performed *ab initio* quantum chemical calculations to characterize the geometry and energy of ethanol conformers with high accuracy. In this work, no clear C_2H_5OH lines are detected in L1544. In IRAS4A and SVS13A, multiple transitions of ethanol are clearly identified. Three possible transitions of C_2H_5OH are detected toward B1-b. However, the transition at 135.989923 GHz is below 3σ, and the other transition at 270.444085 GHz is blended. Only one unblended transition at 131.502781 GHz is detected. Therefore, we consider ethanol to be tentatively detected in this source and derive an upper limit of column density $\sim 1.0 \times 10^{13}$ cm^{-2} (see Table B1). Figure 1 shows that the abundance is maximum in IRAS4A (class 0). It would form on grain surfaces by radical–radical reactions between C_2H_5 and OH. Das et al. (2018) estimated the binding energies of C_2H_5 and OH to be 2081 and 3781 K, respectively. The absence of C_2H_5OH in the prestellar core may be due to the mobility of these two radicals being limited at low temperatures. Also, the binding energy of ethanol itself is high (Wakelam et al. (2017), 5400 K) to release in the gas phase. A comparatively reduced abundance of C_2H_5OH in the class I stage would be due to a lack of production of it by the radical–radical reaction at such a high temperature and its subsequent destruction after its desorption.

3.1.5. HCCCHO

Propynal (HCCCHO) was discovered in a cold cloud, TMC-1, using the NRAO's 42.7 m radio telescope at Green Bank (Irvine et al. 1988). The first laboratory-based infrared spectra of amorphous and crystalline forms of propynal were presented by Hudson & Gerakines (2019) at multiple temperatures. Due to its band intensity and spectral position, it is an attractive candidate for astronomical searches involving interstellar ice. Here, we identify only three transitions of HCCCHO in L1544. With the IRAM 30 m telescope, Jiménez-Serra et al. (2016) carried out high-sensitivity single-pointing 3 mm observations toward the dust-continuum peak in L1544. They detected a single transition for HCCCHO at 83.775842 GHz. We also identify the same transition ($9_{0,9}$–$8_{0,8}$) along with another two transitions. Our RD analysis yields a column density of 3.2×10^{12} cm^{-2} in L1544. We are not able to identify any clear transitions in other sources. However, we estimate an upper limit of HCCCHO for these sources (see Table B1). Loison et al. (2016) reported a single line at 83.775832 GHz ($9_{0,9}$–$8_{0,8}$) of propynal in B1-b, having the column density of 7.9×10^{11} cm^{-2} but we and Margulès et al. (2020) did not observe this particular transition from the ASAI data. Margulès et al. (2020) estimated an upper limit of HCCCHO based on 102.298 GHz transition, but in our observation, we have seen that this transition is shifted and is also blended with s-propanal. Although the line at 93.043 GHz is slightly shifted

from the peak, it is not blended with any other lines. Therefore, on the basis of this transition, we made an upper limit of column density ($\sim 2.56\times10^{12}$ cm^{-2}) in B1-b.

The variation of abundance of HCCCHO in various phases of star formation is shown in Figure 1 with a green-colored bar. We notice that the abundance is relatively low in L1544. It remains roughly the same in B1-b. In the case of IRAS4A, it increases a little. On the other hand, we get a high abundance in SVS13A.

Given that the majority of the abundances provided here are based on the predicted upper limit of propynal, making a strong statement regarding the evolution related to propynal would not be justified. However, in the ice phase, the formation of HCCCHO can proceed by the following reactions:

$$O + CH_2CCH \rightarrow HCCCHO + H,$$

$$C_2H + H_2CO \rightarrow HCCCHO + H.$$

The binding energy value of the reactants obtained from Das et al. (2018) are 770, 3238, 3315, and 3851 K for O, CH_2CCH, C_2H, and H_2CO, respectively. Therefore, at low temperatures, HCCCHO formation could proceed by oxygen addition, whereas in the warmer region, by C_2H and H_2CO. The highest column density obtained at SVS13A indicates that warm chemistry would be efficient.

3.1.6. CH_3OCH_3

Dimethyl ether (DME) is an asymmetric top molecule with two CH_3 groups, which undergoes large amplitude motion along the CO bond. The two internal rotations cause the splitting of a rotational level into four sub-states AA, EE, AE, and EA. DME was detected in the Orion nebula by Snyder et al. (1974). A gas phase formation route for DME was proposed by Blake et al. (1987). Its presence in high-mass star-forming regions (Turner et al. 1999; Sutton et al. 1995; Nummelin et al. 2000) and low-mass binary systems (Cazaux et al. 2003; Kuan et al. 2004) have been observed. From the experiments, observations, and theoretical perspectives, Peeters et al. (2006) discussed the fate of DME in various astrophysical environments. We have identified only one transition ($3_{1,3}$–$2_{0,2}$) of DME with four sub-states AA, AE, EA, and EE in L1544. The EE and AA sub-states are clearly resolved in our study, whereas the EA and AE are overlapped with each other. It is not possible to perform RD analysis as those sub-states have the same upper-state energy. We estimate a column density of 1.6×10^{12} cm^{-2} from LTE fitting. Jiménez-Serra et al. (2016) also observed the same transition in their work and mentioned a column density of 1.5×10^{12} cm^{-2}. In B1-b, we have identified four similar sub-states identical to those observed in L1544. We derive a column density of 6.0×10^{12} cm^{-2} in B1-b from LTE fitting. In IRAS4A, we have observed four unblended transitions, and each of them consists of four sub-states, but they are overlapped with each other. The integrated intensity is obtained with Gaussian fitting and then divided according to their $S\mu^2$ values (Shimonishi et al. 2016). The transitions with maximum intensity among these sub-states are considered for the RD analysis to calculate the rotation temperature and column density. Only these transitions are noted in Table A1. We get a rotational temperature of 61.1 K and column density of 1.2×10^{13} cm^{-2} for this species in this source. The observed transitions of DME in SVS13A have asymmetric line profiles (transitions are not mentioned here; see Bianchi et al. 2019), and hence Gaussian fitting is not possible for these types of transitions. Bianchi et al. (2019) have calculated the column density of DME for an asymmetric line profile (see method described in Appendix A1 of Bianchi et al. 2019). They used a source size of 0.3″ to derive the column density (1.4×10^{17} cm^{-2}) of this species. We use their value after scaling by beam filling factor[13] considering the source size 30″ and the obtained value is $\sim 1.4 \times 10^{13}$ cm^{-2}. We also perform LTE fitting and get a good fit with a column density a few times higher than the scaled value. We use the above-mentioned scaled value in this work.

The variation of the abundance of DME in different sources which are in different phases of star formation is shown in Figure 1 using a magenta-colored bar. We also observed a rising tendency from the L1544 to the IRAS4A and IRAS16293-2422 for DME, similar to what was shown with methanol, acetaldehyde, and methyl formate. Whereas its value gets decreased in SVS13A.

DME is considered to be formed either in the grain surface (Cuppen et al. 2017) or gas phase (Balucani et al. 2015). Both the hydrogenation and radical–radical pathways were involved in the ice phase formation of DME:

$$CH_3CHO + H \rightarrow CH_3OCH_2,$$

$$CH_3OCH_2 + H \rightarrow CH_3OCH_3,$$

$$CH_3 + CH_3O \rightarrow CH_3OCH_3.$$

Both the hydrogenation and the radical–radical route form dimethyl ether. Like methanol, acetaldehyde, and methyl formate, its abundance gradually increases throughout the evolutionary phase up to the class 0 phase and then decreases in the class I phase.

3.2. CH_3CN

Methyl cyanide or CH_3CN is a symmetric-top molecule with a high dipole moment of ∼3.91 Debyes. The K-ladders in the rotational level of CH_3CN can be excited only by collisional excitation. Hence CH_3CN can be a very good tracer to calculate the kinetic temperature of the molecular clouds. We have detected several transitions of CH_3CN in all the selected sources. Similar to CH_3OH and CH_3CHO, for CH_3CN, a two-component fit is required for the RD of methyl cyanide (see Figure C1 online) in IRAS4A, (1) $E_{up} > 50$ K (hot component) and (2) $E_{up} < 50$ K (cold component). RD analysis yields a temperature of 61.2 K for the high excitation lines and 25.8 K for the low excitation lines. Similarly, a two-component MCMC fit is performed and yields a temperature of 70.1 and 21.0 K for hot component and cold component, respectively.

Taking the ratio between two transitions of the same frequency band can nullify various uncertainties obtained from observation. Here we used the line ratios of different CH_3CN transitions observed to calculate the kinetic temperature. Different K_a ladders are connected by collisional excitation. The relative population of two K_a ladders follows the Boltzmann equation at kinetic temperature. Considering the selection rules mentioned in Mangum & Wootten (1993), we calculated the line ratio between two transitions. Details of the selection rule and the method are described in Das et al. (2019) and Mondal et al. (2023). Some selected line ratios are

[13] $ff = \frac{\theta_s^2}{\theta_s^2 + \theta_b^2}$

Table 4
Calculation of Kinetic Temperature Using Line Ratio of Observed CH_3CN Transitions

Source	Frequency (GHz)	Quantum No.	E_{up} (K)	$\int T_{mb} dv$ (K km^{-1} s^{-1})	S_{ij}	R	T_k (K)	Average T_k (K)	
	91.979994	5_2–4_2	41.8	0.067	5.78723	$\frac{5_1-4_1}{5_2-4_2}$	184.38		
	91.985314	5_1–4_1	20.4	0.086	6.61439				
	91.985314	5_1–4_1	20.4	0.086	6.61439	$\frac{5_0-4_0}{5_1-4_1}$	6.42		
	91.987087	5_0–4_0	13.2	0.088	2.2051				
	91.979994	5_2–4_2	41.8	0.067	5.78723	$\frac{5_0-4_0}{5_2-4_2}$	23.11		
	91.987087	5_0–4_0	13.2	0.088	2.2051			43.58	$E_{up} < 50$ K
	110.381372	6_1–5_1	25.7	0.114	8.03828	$\frac{6_0-5_0}{6_1-5_1}$	8.04		
	110.383499	6_0–5_0	18.5	0.093	2.6798				
	110.374989	6_2–5_2	47.1	0.109	7.34927	$\frac{6_0-5_0}{6_2-5_2}$	33.64		
	110.383499	6_0–5_0	18.5	0.093	2.6798				
	128.7768817	7_1–6_1	31.9	0.092	9.44898	$\frac{7_0-6_0}{7_1-6_1}$	5.85		
	128.779363	7_0–6_0	24.7	0.105	3.1501				

calculated ($\frac{J1_{k_a}-J2_{k_a}}{J3_{k_{a'}}-J4_{k_{a'}}}$). Using LTE approximation, the ratio (R) between two transitions satisfying the conditions mentioned in Mangum & Wootten (1993) is, $R = S_R \exp(D/T_K)$, where $D = E(J3, k_{a'}) - E(J1, k_a)$ and $S_R = \frac{S_{J1k_a}}{S_{J3k_{a'}}}$.

Under the LTE approximation, as the kinetic temperature is considered equal to the excitation temperature, we calculated the kinetic temperatures for different CH_3CN k-ladder transitions for the sources (L1544, Barnard1 b, IRAS4A, SVS13A) using the above-mentioned formula. Calculated values of kinetic temperatures for all the CH_3CN transitions are mentioned in Table 4. In Figure 2, we plot the average kinetic temperature obtained from these calculations for the transitions having $E_{up} > 50$ K with the solid blue line, and the dashed blue line in Figure 2 is the same for transitions having $E_{up} < 50$ K.

3.3. Abundance Variation in Different Sources

We found a steadily increasing abundance from L1544 to IRAS4A and peaked at IRAS16293-2422 for CH_3OH, CH_3CHO, CH_3OCHO, C_2H_5OH, CH_3OCH_3, and CH_3CN and a reduced abundance in SVS13A. In contrast, the abundance of HCCCHO shows an increasing trend up to the SVS13A. The trend obtained with HCCCHO is based on the upper limit derived for most of the sources except L1544. In the case of C_2H_5OH, we could not even estimate an upper limit in L1544.

Scibelli & Shirley (2020) noticed that CH_3OH and CH_3CHO formed early and often in the starless prestellar stages and they proposed a chemical link between them at the early stages. However, this proposed linkage in the prestellar cores is yet to be observationally supported by the higher spatial resolution map. They pointed out the chemical linkage between CH_3OH and CH_3CHO by the gas phase reaction: $CH + CH_3OH \rightarrow CH_3CHO + H$. This reaction was experimentally studied by Johnson et al. (2000), who found it to be barrierless. Vasyunin et al. (2017) considered this reaction for their chemical modeling of the prestellar core. However, in the UMIST database, this reaction is considered above 298 K only. In the Kinetic Database for Astrochemistry database, this reaction yields, $CH + CH_3OH \rightarrow CH_3 + H_2CO$ in the 10–300 K range.

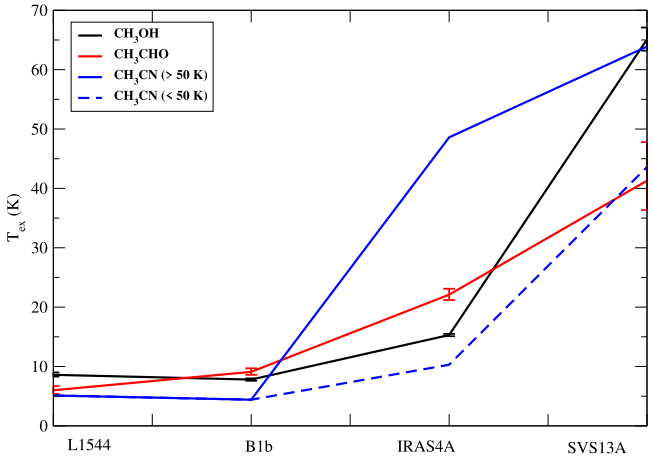

Figure 2. Excitation temperature derived from rotation diagram for methanol (in black) and acetaldehyde (in red), respectively. Vertical lines represent the corresponding errors. Kinetic temperature calculated from Table 4 using CH_3CN transitions for high-temperature (solid blue) and low-temperature (dashed blue) components present in IRAS4A and SVS13A.

The hydrogen column density in each source is required to derive the abundances of the species and look out for their linkage with the various evolutionary phases, if any. For the reliability of the abundance derivation from the obtained column density, we use the hydrogen column density obtained from a beam size comparable to the source size of the molecule (see Section 2.3). As our beam size varies from 30″ to 9″ in our frequency range, we could not resolve the molecular emission originating from the core. To have an idea, we plot the rotational temperature of two species and the kinetic temperature obtained from *k*-ladder calculation for CH_3CN (details in Section 3.2) in all our sample sources. As usual, we found an increased temperature (see Figure 2) from L1544 to SVS13A. Moreover, we studied a particular transition of a species that is common in all the sources. Only one transition (96.755501 GHz) of CH_3OH is present in all the sources. We plot the integrated intensity of this transition of CH_3OH, and it is presented in Figure 3. It implies that the integrated intensity also shows a similar trend with the different sources at different

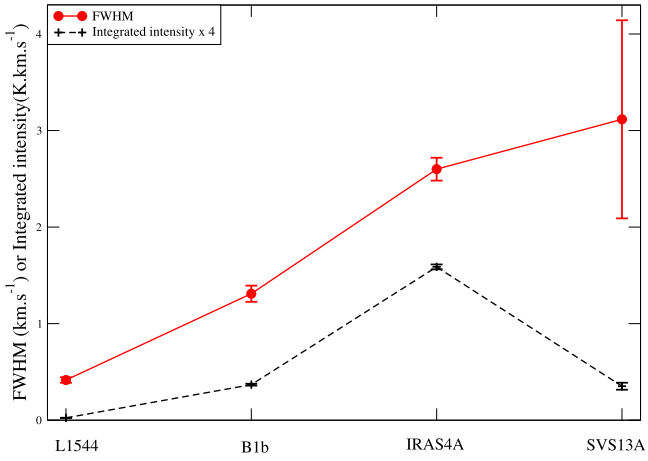

Figure 3. FWHM (red line) and integrated intensity (black-dashed) for 96.755501 GHz transition of methanol. The vertical lines represent the error bars.

stages as it was obtained for the abundances. Additionally, for acetaldehyde, we identified a transition at 211.2738 GHz for all the sources except SVS13A. It shows an increasing trend. In IRAS4A and SVS13A, we identified a transition at 216.5819 GHz and obtained a reduced integrated intensity in SVS13A compared to IRAS4A. Thus, the adopted N(H_2) may not only be responsible for the obtained abundance trend.

Further, we check whether this transition is affected by any of the physical properties of the source. Hence, we plot the variation of FWHM of this transition (96.7555 GHz) for all the sources (see Figure 3). It depicts a steadily increasing trend from L1544 to SVS13A, and its value is comparable to the other observed transitions.

Since all these sources have different luminosity, in Section 3.4, we discuss the link between the obtained abundances and source luminosity.

Except for the L1544, all our sample sources have multiple cores. The targeted position of all the sample sources in ASAI data is mentioned in Table 1. Our observed beam includes all the cores presented in each source, even with the highest frequency of our observation. So, we need to check whether any chemical differentiation is present among the cores of each source and confirm that these cores follow the similar trend that we have obtained. Therefore, the high-resolution interferometric data is required to verify the obtained trend for different sources in different stages. Since the analysis of the interferometric observation is out of scope for this paper, we discuss the interferometric observational results obtained by various authors in these sources in Section 3.4.1.

3.4. Luminosity Effect

Source luminosity or bolometric luminosities may indicate the different evolutionary stages of star formation (Myers et al. 1998). The luminosity considered for L1544, B1-b, IRAS4A, and SVS13A are 1 $L_\odot$, 0.77 $L_\odot$, 9.1 $L_\odot$, and 34 $L_\odot$, respectively (Doty et al. 2005; Lefloch et al. 2018). Since the luminosity of SVS13A is much higher than the other sources considered here, we consider another object, IRAS16293-2422, lying between the IRAS4A and SVS13A to infer the trend related to the luminosity. IRAS16293-2422 is a solar-type class 0 protostar in the eastern part of the ρ Ophiuchi star-forming region at a distance of 120 pc. It has a bolometric luminosity of 22 $L_\odot$. We consider the obtained abundance of methanol, acetaldehyde, methyl formate, dimethyl ether, and methyl cyanide for this source from Cazaux et al. (2003). The abundances of acetaldehyde, methyl formate, and dimethyl ether for this source were derived from the IRAM 30 m data, whereas methanol is from the the James Clerk Maxwell Telescope. Figure 4 depicts the luminosity effect on the molecules considered in this study. The abundances obtained from RD analysis are shown with solid red circles, the MCMC method with solid blue circles, and the data obtained from Cazaux et al. (2003), IRAS 16293-2422 with magenta crosses in Figure 4. The black solid squares are the values obtained by using the upper limit. It shows a similar behavior as discussed in Figure 1. In the case of IRAS 16293-2422, compared to another class 0 object, IRAS4A, a higher column density of these species was obtained by Cazaux et al. (2003). It may be due to a higher luminosity ($\sim$22 $L_\odot$) for IRAS 16293-2422 compared to IRAS4A ($\sim$9.1 $L_\odot$).

Since there are considerable uncertainties in deriving the abundances, it is beneficial to see the molecular ratio of some specific pairs to constrain our understanding better. Multi-line observations of methanol and several COMs toward the two low-mass protostars NGC 1333-IRAS2A and NGC 1333-IRAS4A with the Plateau de Bure Interferometer at an angular resolution of 2″ were carried out by Taquet et al. (2015). They calculated the ratio in column density of CH_3OCH_3 to C_2H_5OH in low-mass protostar IRAS4A is about 0.7 considering the source size 0.5″. In our case, we are getting this ratio with a similar value of 0.7 from the rotation diagram analysis values of IRAS4A. Figure 5 shows the abundance ratio with respect to methanol plotted with the luminosity of the sources. We did not find any specific trend by plotting the molecular ratio. But we found that methanol remains the most abundant among the species studied here (ratios are <1 except for HCCCHO). The first panel of Figure 5 displays the variation of the abundance ratio of acetaldehyde and methanol with luminosity. The ratio remains roughly invariant in IRAS4A, IRAS16293-2422 (class 0), and SVS13A (class I phase). The ratio between methyl formate and methanol in the second panel and between ethanol and methanol in the third panel of Figure 5 shows a similar nature.

3.4.1. Interferometric Observations

It is well known that the evolution of COMs is linked with various evolutionary stages of star formation. We use the large program ASAI data to examine this aspect. We also include the previous interferometric observation to consolidate the obtained trend. Figure 6 shows the obtained abundance trend with the interferometric observation. In Table 5, we have noted the abundances and H_2 column density obtained with the interferometric observations.

There is considerable uncertainty in deriving the abundances of these molecules from the obtained column density. Marcelino et al. (2018b) presented the ALMA Band 6 spectral line observations at the angular resolution of $\sim$0.6″ toward B1-b. They extracted the spectra toward both protostars, B1b-S and B1b-N. However, it was found that B1b-S is rich in COMs, whereas B1b-N is free of COM emission. They derived the column densities of $^{13}CH_3OH$ for source sizes of 0.35″. We utilize a value of $^{12}C/^{13}C = 60$ in deriving the column density of $^{12}CH_3OH$ from this. They also derived the column density of CH_3CHO, CH_3OCH_3, CH_3OCHO, and N(H_2) for a source size

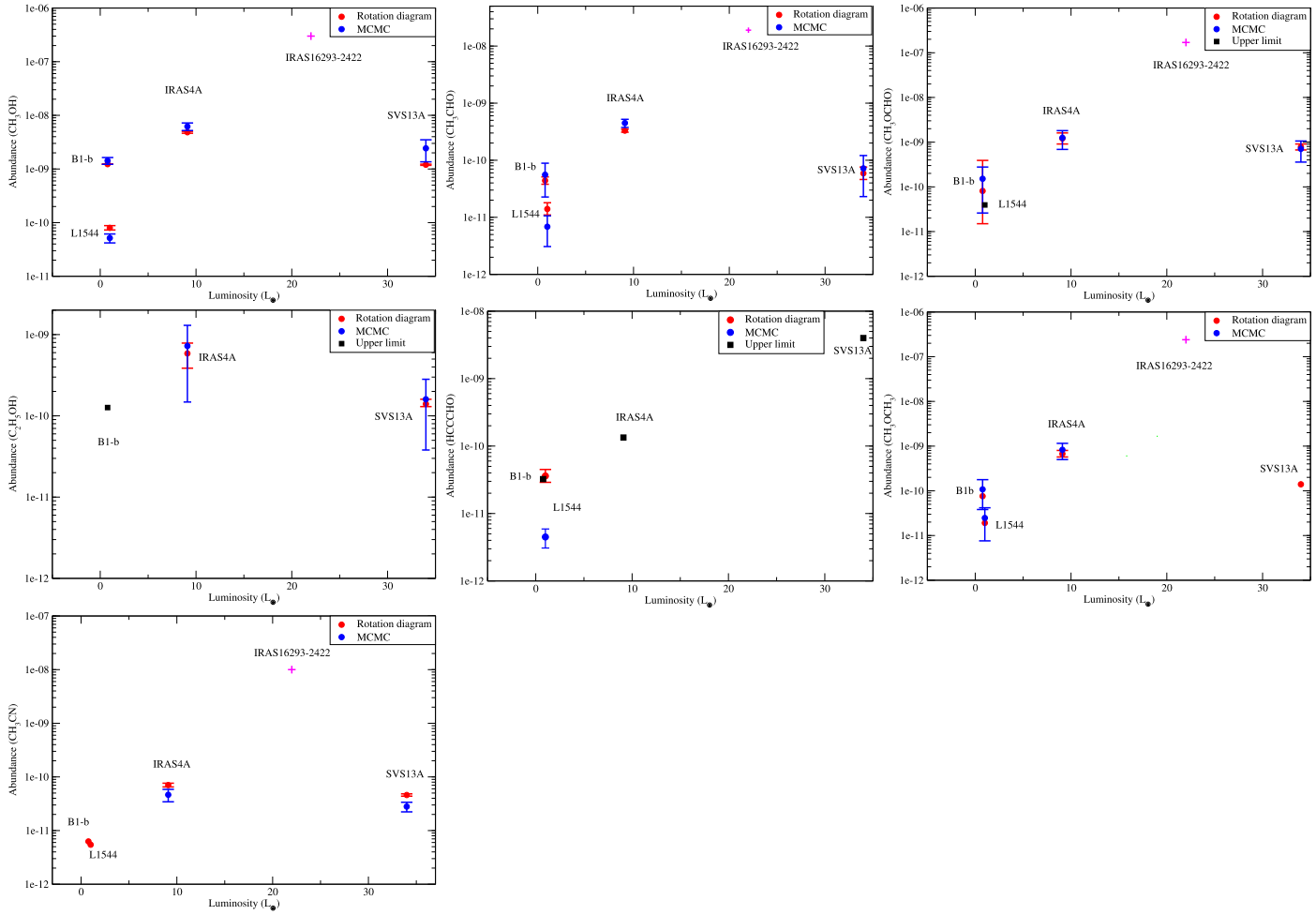

Figure 4. Abundance variation of CH_3OH, CH_3CHO, CH_3O-CHO, C_2H_5OH, HCCCHO, CH_3OCH_3, and CH_3CN shown with source luminosity. The red circle represents the value obtained from the RD, and the blue circle represents the same obtained from MCMC. The solid black squares represent the same calculated using upper limits. The plus sign (magenta) represents the abundance for IRAS4A 16293-2422 (22 $L_{\odot}$) taken from Cazaux et al. (2003). The vertical lines represent the error bars.

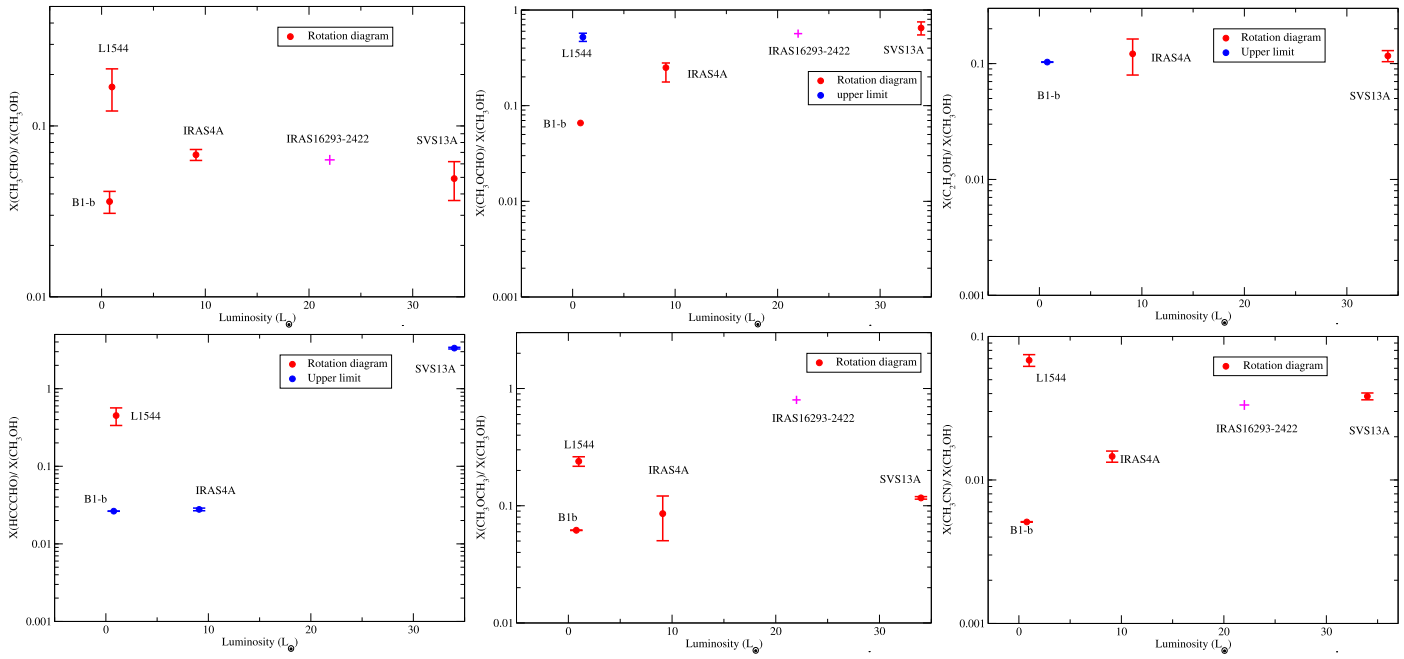

Figure 5. The abundance ratios of CH_3CHO, CH_3OCHO, C_2H_5OH, HCCCHO, CH_3OCH_3, and CH_3CN w.r.t. methanol (CH_3OH) plotted with source luminosity. The red circles represent the value obtained from the RD, and the blue circles represent the same obtained from the upper limits. The plus sign (magenta) represents the abundance obtained for IRAS4A 16293-2422 (22 $L_{\odot}$) taken from Cazaux et al. (2003). Vertical lines represent the error bars.

Table 5
Column Density of Observed Molecules Obtained from Interferometric Observations

Sources	Column density [abundance] in the form of a(b) = a × 10^b				$N(H_2)$ (cm^{-2})
	CH_3OH	CH_3CHO	CH_3OCH_3	CH_3OCHO	
B1-b-S	3.0(17)[a][3.0(− 8)]	1.6(14)[a][1.6(−11)]	1.0(16)[a][1.0(−9)]	5.0(15)[a][5.0(−10)]	1.1(25)[a]
IRAS4A2	6.0(17)[b][2.4(−7)]/ 1.0(19)[c][4.0(−6)]	2.7(16)[b][1.1(−8)]	6.0(16)[b][2.4(-8)]	8.9(16)[b][3.5(−8)]	2.5(24)[f]
IRAS16293-2422 B	1.0(19)[g][8.3(−7)]	1.2(17)[g][1.0(−8)]	2.4(17)[g][2.0(−8)]	2.6(17)[g][2.2(−8)]	1.2(25)[h]
VLA4A	6.0(18)[d][5.5(−7)]	2.4(16)[d][2.2(−9)]	7.5(16)[d][6.8(−9)]	4.2(17)[e][3.8(−8)]	1.0(25)[f]
VLA4B	5.0(18)[d][4.5(−7)]	1.1(16)[d][1.0(−9)]	1.0(17)[d][9.0(−9)]	2.5(17)[e][2.3(−8)]	1.0(25)[f]

Notes.
[a] Marcelino et al. (2018b),
[b] Belloche et al. (2020),
[c] De Simone et al. (2020),
[d] Bianchi et al. (2022a),
[e] Diaz-Rodriguez et al. (2022),
[f] López-Sepulcre et al. (2015),
[g] Jørgensen et al. (2018),
[h] Jørgensen et al. (2016).

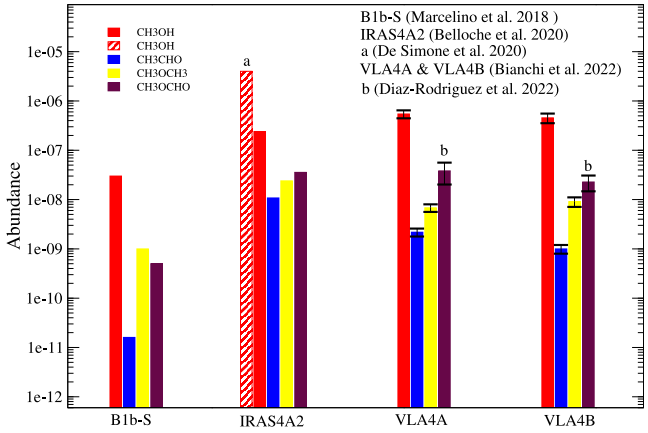

Figure 6. Abundance variation of CH_3OH, CH_3CHO, CH_3OCH_3, and CH_3OCHO obtained from interferometric observation. Black vertical lines represent the error bar.

of 0.60″. In the case of IRAS4A2, the column density is derived from the 0.35″ region (Belloche et al. 2020). De Simone et al. (2020) obtained a very high column density ($\sim 10^{19}$ cm^{-2}) for methanol with a source size of 0.24″. In deriving the abundances of this region, we use a H_2 column density of 2.5×10^{24} cm^{-2} (López-Sepulcre et al. 2015) obtained from the 0.5″ component.

For IRAS16293-2422 B, the column density of these molecules are taken from Jørgensen et al. (2018) for a source size of 0.5″. The column density of CH_3CN is taken from Calcutt et al. (2018). For hydrogen column density, we used a value of 1.2×10^{25} cm^{-2} (Jørgensen et al. 2016).

For SVS13A, the column density of CH_3OH, CH_3CHO, and CH_3OCH_3 are taken from Bianchi et al. (2022a). They observed SVS13A with an angular resolution of 0.106″. The column density of CH_3OCHO is taken from Diaz-Rodriguez et al. (2022) with beam size regions 0.16″ 16×0.08″ toward each component. The H_2 column density of $\sim 1.1 \times 10^{25}$ cm^{-2} is taken from López-Sepulcre et al. (2015) for compact component size of 1.0″.

Figure 6 clearly shows that the general trend (abundances gradually increased up to the class 0 stage and then decreased for the class I phase) obtained for the ASAI survey was also obtained with the interferometric observations.

4. Conclusion

Here, we analyze the ASAI large program data for five sources to understand the chemical and physical evolution of solar-type star-forming regions. We identify CH_3OH, CH_3CHO, CH_3OCHO, C_2H_5OH, HCCCHO, CH_3OCH_3, and CH_3CN in some of these sources we have considered. Observing these COMs in these four sources gave us a transparent view of evolutionary inheritance. The following are our initial findings in this article:

1. An extensive study of the ASAI large program samples identifies many species with different transitions. We employ various LTE methods to measure excitation temperature and column density of a species. For the very first time in B1-b, we tentatively identify some transitions of C_2H_5OH with an upper limit of column density 1.0×10^{13} cm^{-2}.
2. We noticed a comparatively enhanced column density of these species at the FHSC phase compared to the prestellar core. Moreover, no significant difference between class 0 (IRAS4A) and class I phase (SVS13A) has been observed. The two class 0 objects IRAS4A and IRAS 16293-2422 show a significant difference (possibly because of the noticeable difference in luminosity). Abundances of the COMs gradually increase from the L1544 to IRAS16293-2422 and then decrease for SVS13A (Figure 1), except HCCCHO (upper limit). A similar trend is obtained by considering the beam dilution effect (Figure E1) and interferometric data from the literature (Figure 6).

3. We found a trend in the obtained FWHM for a particular transition of methanol. It seems to increase steadily from L1544 (prestellar core) to SVS13A (class I). It also indicates a steady increase of FWHM with the luminosity of the sources.

Although the comparison focuses on only one source of each category, we cannot draw a clear conclusion about the observed trend. More observations of various sources in different stages of low-mass star formation with high spatial and angular resolution are needed to draw a reliable picture of the chemical evolution during the solar-type star formation process.

Acknowledgments

This paper is based on the observations carried out as part of the Large Program ASAI (project number 012-12) using the IRAM 30 m telescope. IRAM is supported by INSU/CNRS (France), MPG (Germany), and IGN (Spain). B.B. gratefully acknowledges the DST, India's Government, for providing financial assistance through the DST-INSPIRE Fellowship (IF170046) scheme. S.K.M. acknowledges the CSIR fellowship (File no. 09/904(0014)/2018-EMR-I). R.G. acknowledges support from the Higher Education Department of the Government of West Bengal. P.G. acknowledges support from a Chalmers Cosmic Origins postdoctoral fellowship. This work was supported by the India–Japan Science Cooperative Program between DST and JSPS, grant No. JPJSBP120207703 and DST/INT/JSPS/P-319/2020. T.S. acknowledges the support from JSPS KAKENHI grant Nos. JP20H05845A and JP21H01145.

Appendix A
Observed Transitions

All the line parameters of observed molecules, such as molecular transitions (quantum numbers) along with their rest frequency(ν), line width (FWHM, ΔV), integrated intensity ($\int T_{mb} dV$), upper state energy (E_u), V_{LSR}, and transition peak line intensity are presented in Table A1 below.

Table A1
Observed Transitions Toward Some Sources

Species	Tag (Database)	Source	Frequency (GHz)	E_{up} (K)	Quantum No.	A_{ij} (s^{-1})	V_{LSR} (km s^{-1})	T_{peak} (K)	FWHM (km s^{-1})	$\int T_{mb} dV$ (K km^{-1} s^{-1})
CH_3OH (methanol)	32003 (Jet Propulsion Laboratory)	L1544	84.521172	40.4	$5_{-1,0}$–$4_{0,0}$	1.97×10^{-6}	7.240 ± 0.010	0.017 ± 0.001	0.441 ± 0.024	0.008 ± 0.001
			96.744545	20.1	$2_{0,0}$–$1_{0,0}$	3.41×10^{-6}	7.160 ± 0.020	0.109 ± 0.001	0.358 ± 0.004	0.042 ± 0.001
			96.755501	28.0	$2_{1,0}$–$1_{1,0}$	2.62×10^{-6}	7.070 ± 0.010	0.013 ± 0.001	0.416 ± 0.029	0.006 ± 0.001
			97.582798	21.5	$2_{1,-0}$–$1_{1,-0}$	2.6×10^{-6}	7.180 ± 0.010	0.019 ± 0.001	0.428 ± 0.021	0.009 ± 0.001
		B1-b	96.739358	12.5	$2_{-1,0}$–$1_{-1,0}$	2.56×10^{-6}	6.641 ± 0.002	1.243 ± 0.003	1.355 ± 0.005	1.793 ± 0.010
			96.741371	6.9	$2_{0,+0}$–$1_{0,+0}$	3.41×10^{-6}	6.615 ± 0.001	1.694 ± 0.003	1.365 ± 0.003	2.462 ± 0.010
			96.744545	20.1	$2_{0,0}$–$1_{0,0}$	3.41×10^{-6}	6.606 ± 0.007	0.306 ± 0.003	1.365 ± 0.018	0.445 ± 0.010
			96.755501	28.0	$2_{1,0}$–$1_{1,0}$	2.62×10^{-6}	6.569 ± 0.033	0.066 ± 0.003	1.310 ± 0.084	0.092 ± 0.010
			108.893945	13.1	$0_{0,0}$–$0_{1,-1}$	1.47×10^{-5}	6.565 ± 0.005	0.377 ± 0.003	1.371 ± 0.013	0.550 ± 0.009
			145.093754	27.0	$3_{0,0}$–$2_{0,0}$	1.23×10^{-5}	6.671 ± 0.003	0.479 ± 0.003	0.950 ± 0.008	0.484 ± 0.007
			145.103185	13.9	$3_{0,+0}$–$2_{0,+0}$	1.23×10^{-5}	6.718 ± 0.001	2.316 ± 0.003	1.005 ± 0.002	2.478 ± 0.007
			157.270832	15.4	$1_{0,0}$–$1_{-1,0}$	2.21×10^{-5}	6.513 ± 0.002	0.896 ± 0.003	1.012 ± 0.004	0.965 ± 0.007
			157.276019	20.1	$2_{0,0}$–$2_{-1,0}$	2.18×10^{-5}	6.533 ± 0.002	0.583 ± 0.003	0.978 ± 0.006	0.607 ± 0.006
			165.050175	23.3	$1_{1,0}$–$1_{0,0}$	2.35×10^{-5}	6.476 ± 0.004	0.334 ± 0.003	0.878 ± 0.010	0.312 ± 0.006
			165.061130	28.0	$2_{1,0}$–$2_{0,0}$	2.34×10^{-5}	6.474 ± 0.005	0.314 ± 0.003	0.905 ± 0.011	0.302 ± 0.006
			165.099240	34.9	$3_{1,0}$–$3_{0,0}$	2.33×10^{-5}	6.524 ± 0.009	0.189 ± 0.002	1.201 ± 0.023	0.242 ± 0.008
			170.060592	36.2	$3_{2,0}$–$2_{1,0}$	2.55×10^{-5}	6.683 ± 0.003	0.510 ± 0.003	0.742 ± 0.006	0.403 ± 0.006
			213.427061	23.3	$1_{1,0}$–$0_{0,0}$	3.37×10^{-5}	6.580 ± 0.002	0.354 ± 0.002	0.903 ± 0.005	0.341 ± 0.004
			254.015377	20.0	$2_{0,0}$–$1_{-1,0}$	1.90×10^{-5}	6.621 ± 0.002	0.427 ± 0.001	1.035 ± 0.005	0.471 ± 0.004
			261.805675	28.0	$2_{1,0}$–$1_{0,0}$	5.57×10^{-5}	6.623 ± 0.002	0.354 ± 0.001	1.005 ± 0.005	0.379 ± 0.003

(This table is available in its entirety in machine-readable form.)

Appendix B
Upper Limit Estimation

For some species, we were unable to identify suitable and multiple transitions to estimate the column density by rotation diagram and MCMC method. In Table B1, we note the estimated upper limits of column density for these species. The input parameters used for this estimation are also noted.

Table B1
Estimated Upper Limit of Column Density

Molecules	Source	Frequency (GHz)	Quantum No.	E_{up} (K)	A_{ij} (s^{-1})	N_{tot} (cm^{-2})	T_k (K)
CH_3OCHO	L1544	90.227659	$8_{0,8}$–$7_{0,7}$, (E)	20.1	1.05×10^{-5}	3.7×10^{12}	10.0
C_2H_5OH	B1-b	131.502781	$6_{3,4}$–$6_{2,5}$, $v_t = 2$–2	28.9	1.27×10^{-5}	1.0×10^{13}	20.0
HCCCHO	B1-b	93.0432843	$10_{0,10}$–$9_{0,9}$	24.6	2.55×10^{-5}	2.56×10^{12}	20.0
	IRAS4A	111.53912	$12_{0,12}$–$11_{0,11}$	34.8	4.43×10^{-5}	3.9×10^{12}	40.0
	SVS13A	236.6916499	$21_{4,17}$–$22_{3,20}$	152.0	4.96×10^{-6}	4.00×10^{14}	100.0

Appendix C
Rotational Diagram

For the optically thin transitions, upper-state column density ($N_u^{\rm thin}$) can be expressed as (Goldsmith & Langer 1999),

$$\frac{N_u^{\rm thin}}{g_u} = \frac{3k_{\rm B}\int T_{\rm mb}dV}{8\pi^3\nu S\mu^2}, \quad \text{(C1)}$$

where g_u is the degeneracy of the upper state, $k_{\rm B}$ is the Boltzmann constant, $\int T_{\rm mb}dV$ is the integrated intensity, ν is the rest frequency, μ is the electric dipole moment, and S is the transition line strength. Under LTE conditions, the total column density ($N_{\rm total}$) can be written as,

$$\frac{N_u^{\rm thin}}{g_u} = \frac{N_{\rm total}}{Q(T_{\rm rot})}\exp(-E_u/k_{\rm B}T_{\rm rot}), \quad \text{(C2)}$$

where $T_{\rm rot}$ is the rotational temperature, E_u is the upper-state energy, and $Q(T_{\rm rot})$ is the partition function at rotational temperature. This can be rearranged as,

$$ln\left(\frac{N_u^{\rm thin}}{g_u}\right) = -\left(\frac{1}{T_{\rm rot}}\right)\left(\frac{E_u}{k}\right) + ln\left(\frac{N_{\rm total}}{Q(T_{\rm rot})}\right). \quad \text{(C3)}$$

There is a linear relationship between the upper-state energy and column density at the upper level. The column density and rotational temperature are extracted from the RD.

The RD analysis can only be performed when multiple transitions (>2) with different upstate energy of a molecule are observed. The estimated rotational temperature ($T_{\rm rot}$) and the column densities are mentioned in Table C1. In some cases (IRAS4A for CH_3OH, CH_3CHO and for CH_3CN), two temperature components are obtained from the RD. Details about the components are mentioned in the main text. The error bars (vertical bars) in RDs are the absolute uncertainty in a log of (N_u/g_u), which arises from the error of the observed integrated intensity that we measured using a single Gaussian fitting to the observed profile of each transition.

Table C1
Results Obtained with the Rotational Diagram Analysis

Molecules	Source	$N_{\rm tot}$ ($\rm cm^{-2}$)	$T_{\rm rot}$ (K)	Abundance
CH_3OH	L1544	$(7.14^{+0.70}_{-0.60}) \times 10^{12}$	$(8.60^{+0.40}_{-0.30})$	$(8.02^{+0.80}_{-0.70}) \times 10^{-11}$
	B1-b	$(9.73^{+0.05}_{-0.04}) \times 10^{13}$	$(7.80^{+0.20}_{-0.20})$	$(1.23^{+0.01}_{-0.01}) \times 10^{-9}$
	IRAS4A	$(1.42^{+0.03}_{-0.02}) \times 10^{14}$	$(15.30^{+0.20}_{-0.20})$	$(4.83^{+0.02}_{-0.02}) \times 10^{-9}$
		$(1.41^{+0.04}_{-0.04}) \times 10^{14}$	$(43.30^{+0.80}_{-0.70})$	$(4.83^{+0.04}_{-0.03}) \times 10^{-9}$
	SVS13A	$(1.21^{+0.03}_{-0.03}) \times 10^{14}$	$(65.10^{+2.0}_{-1.9})$	$(1.21^{+0.03}_{-0.03}) \times 10^{-9}$
CH_3CHO	L1544	$(1.25^{+0.37}_{-0.28}) \times 10^{12}$	$5.98^{+0.70}_{-0.57}$	$(1.40^{+0.42}_{-0.32}) \times 10^{-11}$
	B1-b	$(3.48^{+0.55}_{-0.47}) \times 10^{12}$	$9.09^{+0.62}_{-0.55}$	$(4.40^{+0.70}_{-0.60}) \times 10^{-11}$
	IRAS4A	$(9.47^{+0.56}_{-0.52}) \times 10^{12}$	$(22.09^{+1.03}_{-0.94})$	$(3.30^{+0.19}_{-0.18}) \times 10^{-10}$
		$(9.53^{+1.00}_{-0.95}) \times 10^{12}$	$(64.46^{+5.71}_{-4.85})$	$(3.30^{+0.37}_{-0.33}) \times 10^{-10}$
	SVS13A	$(5.89^{+1.60}_{-1.31}) \times 10^{12}$	$(41.33^{+6.51}_{-4.95})$	$(5.90^{+1.70}_{-1.30}) \times 10^{-11}$
CH_3OCHO	L1544	…	…	…
	B1-b	$(6.40) \times 10^{12}$[c]	(15.50^{c})	$(8.10) \times 10^{-11}$[c]
	IRAS4A	$(3.49^{+0.50}_{-0.40}) \times 10^{13}$	$(82.30^{+8.40}_{-7.00})$	$(1.20^{+0.4}_{-0.3}) \times 10^{-9}$
	SVS13A	$(7.78^{+1.30}_{-1.10}) \times 10^{13}$	$(125.60^{+19.80}_{-15.10})$	$(7.78^{+1.30}_{-1.10}) \times 10^{-10}$
C_2H_5OH	L1544	…	…	…
	B1-b	…	…	…
	IRAS4A	$(1.69^{+0.30}_{-0.20}) \times 10^{13}$	$(50.60^{+4.90}_{-4.10})$	$(5.86^{+0.21}_{-0.22}) \times 10^{-10}$
	SVS13A	$(1.37^{+0.20}_{-0.10}) \times 10^{13}$	$(59.00^{+7.40}_{-5.90})$	$(1.37^{+0.27}_{-0.17}) \times 10^{-10}$
HCCCHO	L1544	$(3.16^{+0.80}_{-0.70}) \times 10^{12}$	$(5.60^{+0.30}_{-0.30})$	$(3.55^{+0.90}_{-0.70}) \times 10^{-11}$
	B1-b	…	…	…
	IRAS4A	…	…	…
	SVS13A	…	…	…
CH_3OCH_3	L1544	1.72×10^{12}[a]	…	$(1.93) \times 10^{-11}$
	B1-b	6.12×10^{12}[a]	…	$(7.74) \times 10^{-11}$
	IRAS4A	$(1.20^{+0.40}_{-0.30}) \times 10^{13}$	$(61.10^{+20.11}_{-12.10})$	$(4.14^{+1.30}_{-1.00}) \times 10^{-10}$
	SVS13A	1.41×10^{13}[b]	…	1.41×10^{-10}
CH_3CN	L1544	4.85×10^{11}[a]	…	$(5.45) \times 10^{-12}$
	B1-b	4.95×10^{11}[a]	…	$(6.27) \times 10^{-12}$
	IRAS4A	$(1.78^{+0.17}_{-0.15}) \times 10^{12}$	$(25.78^{+1.9}_{-1.7})$	$(6.10^{+0.59}_{-0.54}) \times 10^{-11}$
		$(2.31^{+0.31}_{-0.28}) \times 10^{12}$	$(61.2^{+5.05}_{-4.34})$	$(8.00^{+1.10}_{-0.96}) \times 10^{-11}$
	SVS13A	$(4.57^{+0.23}_{-0.22}) \times 10^{12}$	$(134.69^{+11.8}_{-10.09})$	$(4.6^{+0.23}_{-0.22}) \times 10^{-11}$

Notes.
[a] Calculated using LTE fitting.
[b] Calculated from Bianchi et al. (2019) and scaled for 30″ beam.
[c] We did not include the errors due to the large uncertainty in data points. The hydrogen column density (N_{H_2}) in L1544, B1-b, IRAS4A and SVS13A are 8.9×10^{22} $\rm cm^{-2}$ (Hily-Blant et al. 2022), 7.9×10^{22} $\rm cm^{-2}$ (Daniel et al. 2013), 2.9×10^{22} $\rm cm^{-2}$ (Maret et al. 2002), 1.0×10^{23} $\rm cm^{-2}$ (Lefloch et al. 1998), respectively.

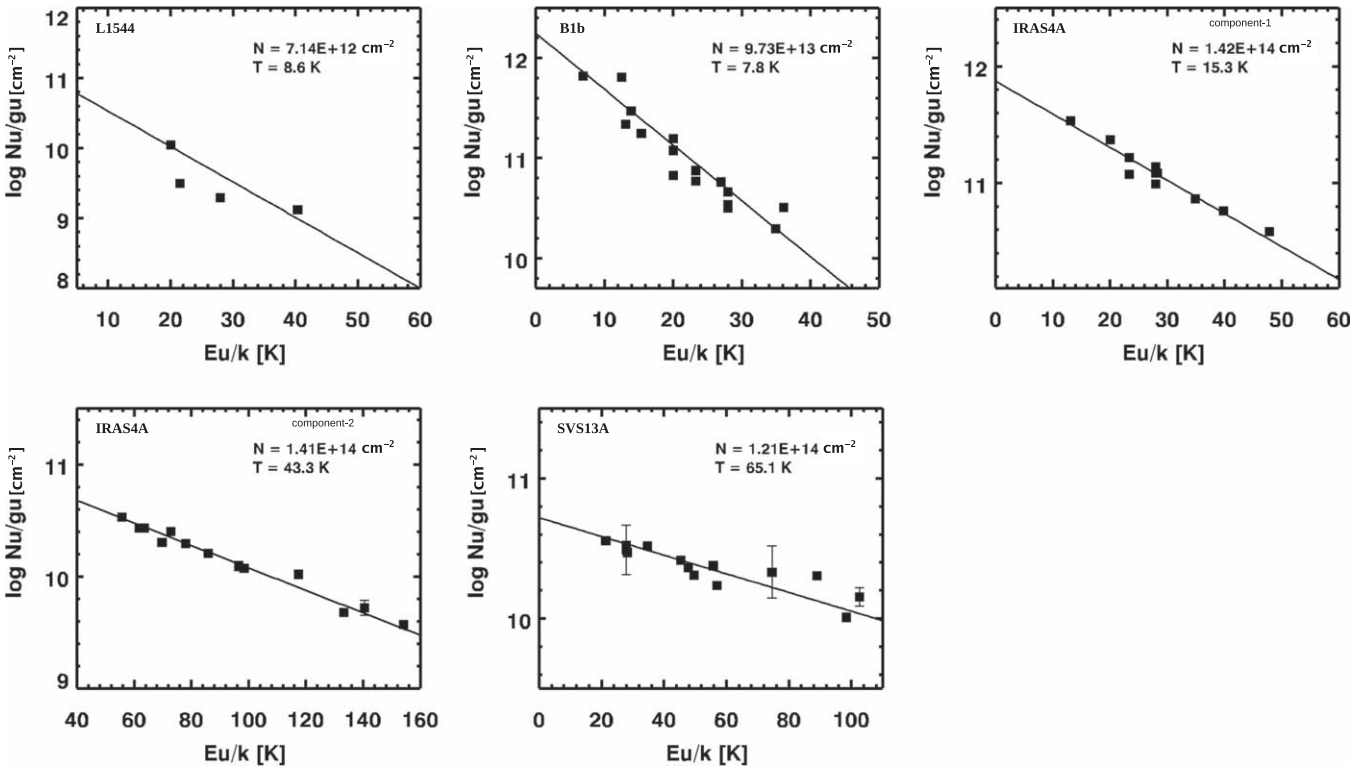

Figure C1. RD for CH_3OH obtained with various sources. The black points are the position of the data points, the vertical bars are the error bars estimated, and the red lines are the fitted lines to the RD. The obtained column densities and the excitation temperatures along with the error bars are mentioned in the top right corner of each box. The complete figure set (20 images) for various sources and molecules (CH_3OH, CH_3CHO, CH_3OCHO, C_2H_5OH, HCCCHO, CH_3OCH_3 $v = 0$ and CH_3CN) is available in the online Journal.

(The complete figure set (20 images) is available.)

Appendix D
MCMC Method

The MCMC method is one of the most important and popular concepts in Bayesian statistics. Understanding the physical conditions in star-forming regions is a challenge nowadays as the chemistry in the star-forming regions are complicated and varies nonlinearly with time and other physical conditions. In astrochemistry, we use many trial and error grid-based analysis using simple statistics. However, when the parameter space is large, heterogeneous, and complex, this approach fails. To interpret the astrochemical conditions a new method using a Bayesian approach, the MCMC method is implemented by an iterative process to solve it using simulation. The MCMC method is an interactive process that goes through all line parameters (e.g., molecular column density, excitation temperature, source size, line width) with a random walk and heads into the solution's space and the final solution is obtained by χ^2 minimization. As well as RD analysis, the MCMC method can be used to obtain the best suitable physical conditions only for those species for which multiple or at least more than two transitions are observed with different upstate energies. The χ^2 is defined as,

$$\chi_i^2 = \sum_{j=1}^{N_i} \frac{(I_{obs,ij} - I_{model,ij})^2}{rms_i^2 + (cal_i \times I_{obs,ij})^2}, \quad \text{(D1)}$$

where, $I_{obs,ij}$ and $I_{model,ij}$ are observed and modeled intensity in the channel j of transition i respectively, rms_i is the rms of the spectrum i, and cal_i is the calibration error. Here, the MCMC method is only used to fit the observed transitions of those species for which multiple transitions are observed. Here we employed the MCMC method from the CASSIS scripting interface to fit the observed lines of those seven COMs (CH_3OH, CH_3CHO, CH_3OCHO, C_2H_5OH, HCCCHO, CH_3OCH_3, CH_3CN), which we have considered toward different star-forming regions. Since we obtained a beam average column density with the RD analysis, we ignored the beam filling factor for the MCMC calculation. In some cases (CH_3OH and CH_3CHO in IRAS4A), we employ a two-component MCMC fitting to have a better match with the observation. The components are considered based on their temperature. Details are described in Section 3. We also kept the local standard of rest (LSR) velocity constant at 7.2, 6.5, 7.2, 2.6, and 8.4 km s^{-1}, respectively, for L1544, B1-b, IRAS4A, L1157-mm, and SVS13A. For the fitting, we varied FWHM, column density, and excitation temperature (T_{ex}) and obtained the best fit parameters from the LTE fitting using MCMC method. All the parameters along with the best fitted values of the physical parameters are noted in Table D1. Spectral fit for all the transitions arose from various molecules are shown in Figure D1 and the online figure set.

Table D1
Summary of the Best Fitted Line Parameters Obtained by Using MCMC Method

Species	Source	Frequency (GHz)	FWHM Range Used (km s^{-1})	Best Fitted FWHM (km s^{-1})	Column Density Range used (cm^{-2})	Best Fitted Column Density (cm^{-2})	T_{ex} Range Used (K)	Best Fitted T_{ex} (K)	Best Fitted V_{LSR} (km s^{-1})	Optical Depth (τ)
CH_3OH	L1544	84.5211								1.98×10^{-3}
		96.7445	0.3–0.5	0.39 ± 0.03	1.0×10^{11}–1.0×10^{14}	$(4.60 \pm 0.92) \times 10^{12}$	3.5–17.0	12.9 ± 3.07	7.2	5.86×10^{-3}
		96.7555								2.44×10^{-3}
		97.5828								3.97×10^{-3}
	B1-b	96.7393								2.08×10^{-1}
		96.7413								5.98×10^{-1}
		96.7445	1.0–3.0	1.50 ± 0.10	1.0×10^{13}–1.0×10^{15}	$(1.60 \pm 0.12) \times 10^{14}$	5.0–25.0	7.27 ± 0.86	6.5	9.83×10^{-2}
		96.7555								2.55×10^{-2}
		108.8939								1.83×10^{-1}
		145.0937								5.11×10^{-2}
		145.1031								2.18×10^{-1}
		157.2708								1.25×10^{-1}
		157.2760	1.0- 3.0	1.05 ± 0.08	1.0×10^{13}–1.0×10^{15}	$(5.90 \pm 0.51) \times 10^{13}$	5.0–25.0	9.06 ± 1.26	6.5	1.23×10^{-1}
		165.0501								5.15×10^{-2}
		165.0611								5.13×10^{-2}
		165.0992								3.31×10^{-2}
		170.0605								3.04×10^{-2}
		213.4270								1.47×10^{-1}
		254.0153	1.0–3.0	1.0 ± 0.09	1.0×10^{13}–1.0×10^{15}	$(1.20 \pm 0.32) \times 10^{14}$	5.0–25.0	6.77 ± 0.95	6.5	1.89×10^{-1}
		261.8056								1.68×10^{-1}
	IRAS4A	96.7555								$1.14 \times 10^{-2}/2.62 \times 10^{-3}$
		108.8939								$1.52 \times 10^{-1}/3.57 \times 10^{-3}$
		143.8657								$3.50 \times 10^{-2}/6.90 \times 10^{-3}$
		155.3208								$2.89 \times 10^{-10}/1.07 \times 10^{-3}$
		155.9975								$1.73 \times 10^{-8}/1.99 \times 10^{-3}$
		156.4889								$6.71 \times 10^{-7}/3.41 \times 10^{-3}$
		156.8285								$1.69 \times 10^{-5}/5.36 \times 10^{-3}$
		157.0486								$2.75 \times 10^{-4}/7.70 \times 10^{-3}$
		157.1789								$2.88 \times 10^{-3}/1.00 \times 10^{-2}$
		165.0501				Component 1				$6.79 \times 10^{-2}/5.78 \times 10^{-3}$
		165.0611	1.0–3.5	3.03 ± 0.27	1.0×10^{13}–1.0×10^{15}	$(1.80 \pm 0.29) \times 10^{14}$	5.0–30.0	5.62 ± 1.68	7.2	$4.94 \times 10^{-2}/8.42 \times 10^{-3}$
		165.0992								$1.99 \times 10^{-2}/9.62 \times 10^{-3}$
		165.6786				Component 2				$7.34 \times 10^{-5}/6.48 \times 10^{-3}$
		166.1690	1.0–3.5	3.50 ± 0.47	1.0×10^{13}–1.0×10^{15}	$(2.00 \pm 0.28) \times 10^{14}$	30.0–70.0	35.14 ± 3.86	7.2	$4.65 \times 10^{-6}/4.66 \times 10^{-3}$
		213.4270								$7.56 \times 10^{-2}/5.13 \times 10^{-3}$
		230.0270								$3.92 \times 10^{-3}/2.88 \times 10^{-3}$
		241.8790								$1.37 \times 10^{-3}/1.05 \times 10^{-2}$
		251.7384								$9.90 \times 10^{-7}/4.28 \times 10^{-3}$
		251.8665								$5.29 \times 10^{-5}/5.01 \times 10^{-3}$
		251.9170								$1.54 \times 10^{-4}/3.63 \times 10^{-3}$
		251.9848								$4.59 \times 10^{-9}/2.33 \times 10^{-3}$
		252.0904								$1.36 \times 10^{-10}/1.49 \times 10^{-3}$

Table D1
(Continued)

Species	Source	Frequency (GHz)	FWHM Range Used (km s^{-1})	Best Fitted FWHM (km s^{-1})	Column Density Range used (cm^{-2})	Best Fitted Column Density (cm^{-2})	T_{ex} Range Used (K)	Best Fitted T_{ex} (K)	Best Fitted V_{LSR} (km s^{-1})	Optical Depth (τ)
		254.0153								$1.13 \times 10^{-1}/3.85 \times 10^{-3}$
		261.8056								$7.95 \times 10^{-2}/8.53 \times 10^{-3}$
	SVS13A	85.5681								3.08×10^{-4}
		96.7555	2.0–4.5	4.04 ± 0.59	1.0×10^{13}–1.0×10^{15}	$(3.00 \pm 2.42) \times 10^{14}$	40.0–200.0	96.72 ± 18.77	8.6	3.51×10^{-4}
		111.2894								3.65×10^{-4}
		143.8657								1.01×10^{-3}
		156.6023	2.0–3.5	3.47 ± 0.39	1.0×10^{13}–1.0×10^{15}	$(2.80 \pm 0.62) \times 10^{14}$	40.0–100.0	96.70 ± 14.03	8.6	1.09×10^{-3}
		218.4400								2.37×10^{-3}
		229.7587								1.93×10^{-3}
		241.7001								2.97×10^{-3}
		241.7913								3.60×10^{-3}
		241.8790	2.0–3.5	3.36 ± 0.24	1.0×10^{13}–1.0×10^{15}	$(1.50 \pm 0.17) \times 10^{14}$	40.0–100.0	68.69 ± 8.41	8.6	2.61×10^{-3}
		243.9157								2.81×10^{-3}
		251.7384								1.92×10^{-3}
		261.8056								1.43×10^{-3}
		266.8381								2.76×10^{-3}
CH_3CHO	L1544	93.5809								1.32×10^{-2}
		93.5952								1.31×10^{-2}
		95.9474	0.3–0.6	0.39 ± 0.09	1.0×10^{11}–1.0×10^{13}	$(6.10 \pm 3.55) \times 10^{11}$	3.5–20.0	6.04 ± 4.42	7.2	1.93×10^{-2}
		95.9634								1.96×10^{-2}
		98.8633								1.25×10^{-2}
		98.9009								1.26×10^{-1}
	B1-b	93.5809								1.65×10^{-2}
		93.5952								1.64×10^{-2}
		95.9634								2.30×10^{-2}
		96.4256	0.5–2.0	1.49 ± 0.36	1.0×10^{11}–5.0×10^{13}	$(4.70 \pm 2.39) \times 10^{12}$	6.0–100.0	7.52 ± 6.61	6.5	5.78×10^{-3}
		96.4755								5.70×10^{-3}
		98.8633								1.59×10^{-2}
		98.9009								1.61×10^{-2}
		138.2849	0.5–1.5	1.38 ± 0.24	1.0×10^{11}–5.0×10^{13}	$(4.10 \pm 2.84) \times 10^{12}$	6.0–100.0	10.81 ± 3.63	6.5	5.08×10^{-3}
		138.3196								5.11×10^{-3}
		152.6352								4.59×10^{-3}
		155.1796								1.81×10^{-3}
	IRAS4A	74.8917								$8.67 \times 10^{-3}/1.89 \times 10^{-4}$
		74.9241								$8.60 \times 10^{-3}/1.88 \times 10^{-4}$
		76.8789								$1.14 \times 10^{-2}/2.13 \times 10^{-4}$
		77.0386								$3.79 \times 10^{-3}/1.41 \times 10^{-4}$
		77.2183								$3.80 \times 10^{-3}/1.41 \times 10^{-4}$
		79.0993								$8.75 \times 10^{-3}/1.98 \times 10^{-4}$
		93.5809								$9.64 \times 10^{-3}/2.85 \times 10^{-4}$
		93.5952								$9.58 \times 10^{-3}/2.85 \times 10^{-4}$

Table D1
(Continued)

Species	Source	Frequency (GHz)	FWHM Range Used (km s^{-1})	Best Fitted FWHM (km s^{-1})	Column Density Range used (cm^{-2})	Best Fitted Column Density (cm^{-2})	T_{ex} Range Used (K)	Best Fitted T_{ex} (K)	Best Fitted V_{LSR} (km s^{-1})	Optical Depth (τ)
		95.9474								$1.22 \times 10^{-2}/3.13 \times 10^{-4}$
		96.2742								$4.56 \times 10^{-3}/2.32 \times 10^{-4}$
		96.4256								$4.56 \times 10^{-3}/2.31 \times 10^{-4}$
		96.4755								$4.51 \times 10^{-3}/2.31 \times 10^{-4}$
		98.8633								$9.56 \times 10^{-3}/2.98 \times 10^{-4}$
		112.248								$9.02 \times 10^{-3}/3.88 \times 10^{-4}$
		112.2545								$8.97 \times 10^{-3}/3.87 \times 10^{-4}$
		133.8305								$8.85 \times 10^{-3}/5.22 \times 10^{-4}$
		138.2849								$6.88 \times 10^{-3}/5.08 \times 10^{-4}$
		138.3196				Component 1				$6.92 \times 10^{-3}/5.08 \times 10^{-4}$
		152.6352	2.0–3.5	3.30 ± 0.22	1.0×10^{12}–1.0×10^{14}	$(1.30 \pm 0.21) \times 10^{13}$	8.0–30.0	11.07 ± 3.48	7.2	$6.27 \times 10^{-3}/6.18 \times 10^{-4}$
		155.3421				Component 2				$2.58 \times 10^{-3}/5.19 \times 10^{-4}$
		168.0934	2.0–3.5	2.3 ± 0.32	1.0×10^{12}–1.0×10^{14}	$(1.10 \pm 0.21) \times 10^{13}$	30.0–80.0	71.2 ± 5.17	7.2	$3.36 \times 10^{-3}/6.66 \times 10^{-4}$
		208.2285								$1.13 \times 10^{-3}/8.04 \times 10^{-4}$
		211.2738								$4.75 \times 10^{-4}/6.92 \times 10^{-4}$
		212.2571								$1.63 \times 10^{-4}/5.68 \times 10^{-4}$
		214.8450								$4.63 \times 10^{-4}/7.00 \times 10^{-4}$
		216.6302								$8.10 \times 10^{-4}/7.85 \times 10^{-4}$
		223.6601								$4.77 \times 10^{-4}/7.99 \times 10^{-4}$
		242.1060								$2.04 \times 10^{-4}/8.02 \times 10^{-4}$
		250.8291								$7.31 \times 10^{-6}/4.55 \times 10^{-4}$
		250.9345								$3.16 \times 10^{-5}/5.94 \times 10^{-4}$
		251.4893								$3.16 \times 10^{-5}/5.95 \times 10^{-4}$
		254.8271								$8.67 \times 10^{-5}/7.22 \times 10^{-4}$
		255.3269								$1.47 \times 10^{-4}/7.97 \times 10^{-4}$
		262.9601								$8.63 \times 10^{-5}/8.02 \times 10^{-4}$
		205.1707								9.80×10^{-4}
	SVS13A	211.2430								8.18×10^{-4}
		211.2738								8.17×10^{-4}
		216.5819	0.5–2.5	2.45 ± 0.33	1.0×10^{12}–1.0×10^{14}	$(7.20 \pm 4.89) \times 10^{12}$	30.0–200.0	45.16 ± 11.4	8.6	9.66×10^{-4}
		230.3019								7.74×10^{-4}
		242.1060								8.51×10^{-4}
		251.4893								5.34×10^{-4}
CH_3OCHO	B1-b	88.8516								1.48×10^{-3}
		90.1457								1.30×10^{-3}
		90.1564	1.0–2.0	1.64 ± 0.21	1.0×10^{11}–1.0×10^{14}	$(1.20 \pm 1.00) \times 10^{13}$	15.0–100.0	18.52 ± 22.81	6.5	1.30×10^{-3}
		100.2946								1.03×10^{-3}
		100.4822								1.49×10^{-3}
		103.4786								1.35×10^{-3}
	IRAS4A	129.2963*								3.92×10^{-4}
		132.9287								4.24×10^{-4}
		135.9219								2.90×10^{-4}

Table D1
(Continued)

Species	Source	Frequency (GHz)	FWHM Range Used (km s^{-1})	Best Fitted FWHM (km s^{-1})	Column Density Range used (cm^{-2})	Best Fitted Column Density (cm^{-2})	T_{ex} Range Used (K)	Best Fitted T_{ex} (K)	Best Fitted V_{LSR} (km s^{-1})	Optical Depth (τ)
		141.0443	1.0–3.0	1.86 ± 0.54	1.0×10^{12}–1.0×10^{14}	$(3.90 \pm 1.54) \times 10^{13}$	30.0–130.0	73.87 ± 24.37	7.2	4.45×10^{-4}
		158.6937								4.53×10^{-4}
		158.7043								4.53×10^{-4}
		200.9563	1.0–3.0	1.35 ± 0.50	1.0×10^{12}–1.0×10^{14}	$(3.40 \pm 1.72) \times 10^{13}$	30.0–130.0	81.32 ± 18.46	7.2	4.21×10^{-4}
		206.6194								5.13×10^{-4}
		216.2165								5.06×10^{-4}
		228.6288								4.28×10^{-4}
		240.0211								4.75×10^{-4}
		247.0441								4.38×10^{-4}
		249.5781								3.57×10^{-4}
	SVS13A	100.4906	1.0–3.0	1.95 ± 0.53	1.0×10^{12}–1.0×10^{15}	$(6.40 \pm 5.17) \times 10^{13}$	40.0–200.0	86.94 ± 33.36	8.6	3.04×10^{-4}
		164.2059								4.73×10^{-4}
		210.4632	1.0–3.0	2.10 ± 0.37	1.0×10^{12}–1.0×10^{15}	$(7.80 \pm 1.88) \times 10^{13}$	40.0–200.0	113.84 ± 23.41	8.6	2.81×10^{-4}
		218.2809								4.15×10^{-4}
		222.4214								2.55×10^{-4}
		269.0780								4.06×10^{-4}
C_2H_5OH	IRAS4A	129.6657	0.4–1.5	1.46 ± 0.26	1.0×10^{12}–1.0×10^{14}	$(2.60 \pm 1.61) \times 10^{13}$	30.0–100.0	60.14 ± 16.62	7.2	2.84×10^{-4}
		133.3234								5.90×10^{-4}
		148.3040								2.76×10^{-4}
		159.4140								2.92×10^{-4}
		205.4584	0.4–0.8	0.74 ± 0.06	1.0×10^{12}–1.0×10^{14}	$(1.60 \pm 0.59) \times 10^{13}$	30.0–100.0	88.46 ± 18.28	7.2	5.22×10^{-4}
		209.8652								2.29×10^{-4}
		227.8919								2.72×10^{-4}
		230.9913								5.63×10^{-4}
	SVS13A	84.5958	0.5–2.0	0.92 ± 0.41	1.0×10^{12}–1.0×10^{14}	$(1.70 \pm 1.59) \times 10^{13}$	10.0–100.0	45.63 ± 17.28	8.6	4.02×10^{-4}
		130.2463								4.64×10^{-4}
		153.4842								5.24×10^{-4}
		205.4584	0.5–2.0	0.97 ± 0.28	1.0×10^{12}–1.0×10^{14}	$(1.50 \pm 0.86) \times 10^{13}$	10.0–100.0	59.58 ± 21.85	8.6	8.26×10^{-4}
		244.6339								2.78×10^{-4}
		270.4441								7.21×10^{-4}
HCCCHO	L1544	83.7758	0.3–0.6	0.43 ± 0.07	1.0×10^{11}–1.0×10^{13}	$(4.00 \pm 1.33) \times 10^{11}$	3.5–20.0	17.40 ± 5.24	7.2	1.43×10^{-3}
		99.0391								6.28×10^{-5}
		102.2980								1.28×10^{-3}
CH_3OCH_3	L1544	99.324362	0.1–1.0	0.41 ± 0.22	1.0×10^{11}–1.0×10^{13}	$(2.20 \pm 1.61) \times 10^{12}$	3.5–20.0	15.47 ± 2.71	7.2	3.66×10^{-4}
		99.324364								5.49×10^{-4}
		99.325217								1.46×10^{-3}
		99.326072								9.15×10^{-4}
	B1-b	99.324362	0.5–1.0	0.9 ± 0.12	6.0×10^{11}–6.0×10^{13}	$(8.50 \pm 5.52) \times 10^{12}$	5.0–25.0	9.85 ± 4.56	6.5	1.49×10^{-3}
		99.324364								2.23×10^{-3}

Table D1
(Continued)

Species	Source	Frequency (GHz)	FWHM Range Used (km s^{-1})	Best Fitted FWHM (km s^{-1})	Column Density Range used (cm^{-2})	Best Fitted Column Density (cm^{-2})	T_{ex} Range Used (K)	Best Fitted T_{ex} (K)	Best Fitted V_{LSR} (km s^{-1})	Optical Depth (τ)
		99.325217								5.95×10^{-3}
		99.326072								3.72×10^{-3}
	IRAS4A	162.5295								5.38×10^{-4}
		209.5156								6.02×10^{-4}
		225.5991	1.0–3.0	2.11 ± 0.35	1.0×10^{12}–1.0×10^{14}	$(2.10 \pm 1.03) \times 10^{13}$	30.0–130.0	45.28 ± 28.29	7.2	5.83×10^{-4}
		241.9465								5.45×10^{-4}
CH_3CN	IRAS4A	73.588799								1.97×10^{-3}
		73.590218								2.96×10^{-3}
		91.979994								8.26×10^{-4}
		91.985314								2.61×10^{-3}
		91.987087								3.83×10^{-3}
		110.364353								3.08×10^{-4}
		110.381372								3.03×10^{-3}
		110.383499								4.38×10^{-3}
		128.757030								3.48×10^{-4}
		128.769436								1.07×10^{-3}
		128.776881				Component 1				3.16×10^{-3}
		128.779363	1.5–3.0	2.9 ± 0.19	1.0×10^{11}–1.0×10^{13}	$(9.9 \pm 3.15) \times 10^{11}$	20.0–50.0	21.02 ± 3.24	7.2	4.54×10^{-3}
		147.163244				Component 2				1.04×10^{-3}
		147.171751	1.5–3.0	2.9 ± 0.12	1.0×10^{11}–1.0×10^{13}	$(1.7 \pm 0.38) \times 10^{12}$	50.0–80.0	70.11 ± 5.32	7.2	3.04×10^{-3}
		147.174588								4.34×10^{-3}
		165.540377								3.21×10^{-4}
		165.556321								9.38×10^{-4}
		165.565891								2.70×10^{-3}
		165.569081								3.84×10^{-3}
		202.320442								2.16×10^{-4}
		220.709016								1.61×10^{-4}
	SVS13A	91.979994								2.705×10^{-4}
		91.985314								3.996×10^{-4}
		91.987087								4.535×10^{-4}
		110.364353								4.281×10^{-4}
		110.374989								3.890×10^{-4}
		110.381372								5.499×10^{-4}
		110.383499								6.162×10^{-4}
		128.776881	1.5–3.5	3.48 ± 0.09	5.0×10^{11}–5.0×10^{13}	$(2.8 \pm 0.57) \times 10^{12}$	40.0–200.0	83.55 ± 19.34	8.6	7.041×10^{-4}
		128.779363								7.832×10^{-4}
		147.171751								8.538×10^{-4}
		165.565891								9.913×10^{-4}
		220.709016								1.210×10^{-3}
		220.730260								9.624×10^{-4}
		220.743010								1.270×10^{-3}
		220.747261								1.394×10^{-3}
		239.119504								9.939×10^{-4}
		257.527383								1.441×10^{-3}

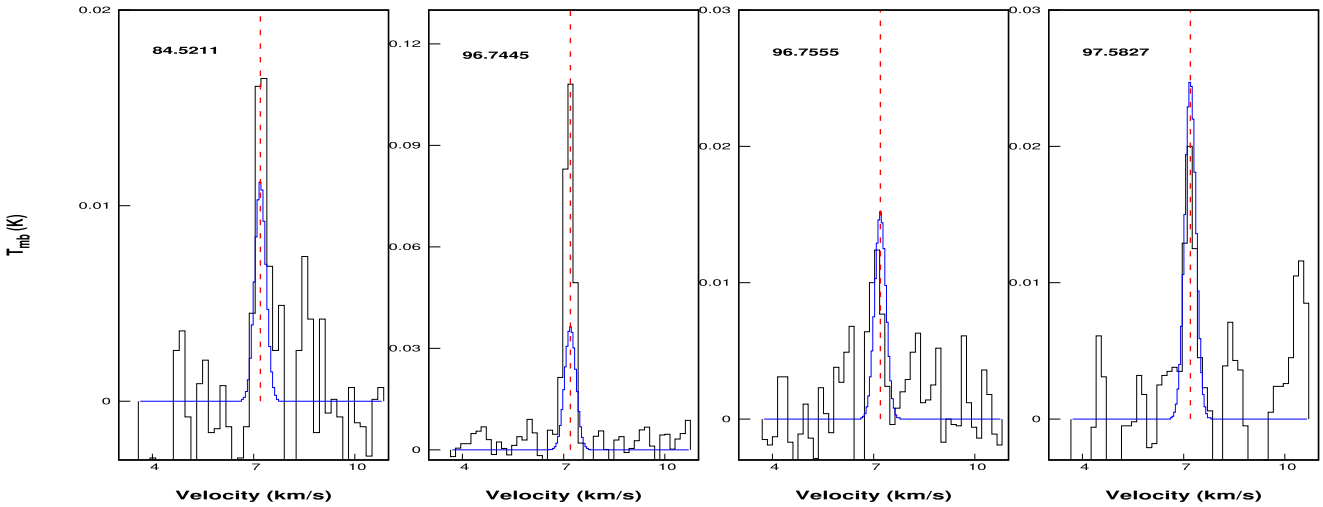

Figure D1. MCMC fitting of the observed transitions of CH_3OH in L1544. Black lines represent the observed spectra, and blue represents the modeled spectral profile. The vertical red dashed line represents the *V*LSR. The complete figure set (13 images) for various sources and molecules is available in the online journal. (The complete figure set (13 images) is available.)

Appendix E
Beam Dilution Effect

The present data have a large frequency width, and the beam size changes significantly. Therefore, we need to assume the size of the emitting region for the COMs and apply the appropriate beam dilution factor for each source to see its effect. Figure E1 shows the abundances (obtained from the RD analysis) at the different evolutionary stages of low-mass star-forming regions by considering the beam dilution effect. Additionally, we note the obtained abundances in Table E1. The obtained intensities in the RD analysis are scaled by considering the beam dilution factor for each source. For simplicity, we consider an average source size, and the choice of source size for each source is justified below.

L1544: Caselli et al. (2019, 2022) obtained a compact component of $\sim$10″ in L1544. Assuming the emission of the COMs from this region, we consider a source size of 10″ (see Figure E1 and in Table E1).

B1-b: Marcelino et al. (2018a) employed a source model with two components; an inner hot and compact component (200 K, 0.35″) and an outer and colder component (60 K, 0.6″) to fit the observed line profiles in B1b-S. Additionally, they considered another component mimicking the envelope at $\sim$10 K. In our analysis, we obtain a rotational temperature $\sim$10 K for all molecules in this source, we consider a source size of 10″, which is comparable to the smallest beam size in this data (see Figure E1).

IRAS16293-2422: We consider the abundances obtained directly from the ALMA Protostellar interferometric line survey (for details, see Section 3.4.1).

IRAS4A: López-Sepulcre et al. (2015) considered a source size of 0.5″ to perform the RD analysis for NH_2CHO and HNCO in IRAS4A. We adopt similar source size of 0.5″ to consider beam dilution effect (see Table E1 and Figure E1).

SVS13A: López-Sepulcre et al. (2015) considered a source size of 1.0″ to perform the RD analysis for NH_2CHO and HNCO in SVS13A and Bianchi et al. (2019) considered a

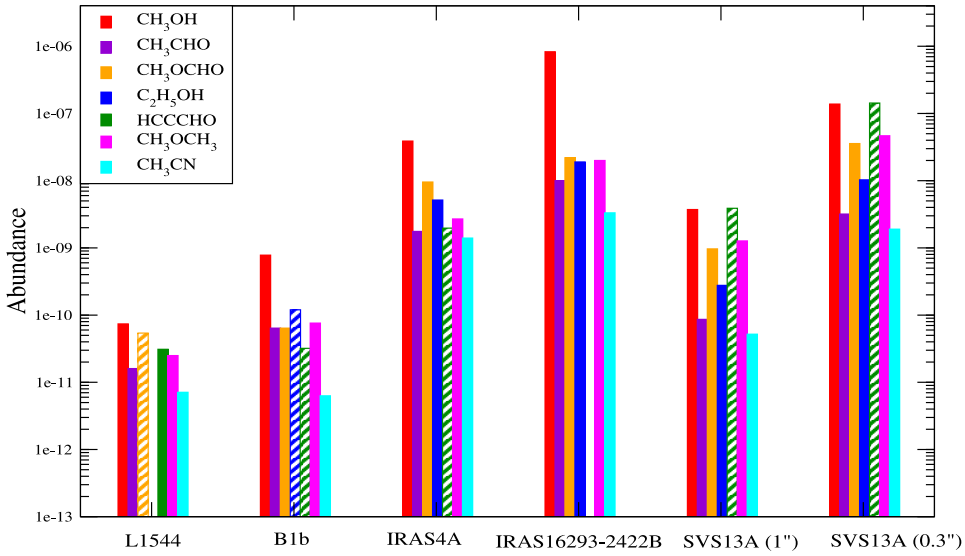

Figure E1. Abundances of the COMs at the different evolutionary stages of low-mass star-forming regions.

Table E1
Column Density and Abundance of the Observed Species Considering the Beam Dilution Factor

Source	Size	$N(H_2)$	Species	Column Density	Abundance
L1544	10″	6.8×10^{23}[e]	CH_3OH	5.0×10^{13}	7.4×10^{-11}
			CH_3CHO	1.1×10^{13}	1.6×10^{-11}
			CH_3OCHO	3.7×10^{13}[a]	5.4×10^{-11}
			C_2H_5OH	…	…
			HCCCHO	2.1×10^{13}	3.1×10^{-11}
			CH_3OCH_3	1.7×10^{13}[b]	2.5×10^{-11}
			CH_3CN	4.85×10^{12}[b]	7.1×10^{-12}
B1-b	10″	7.9×10^{23}[f]	CH_3OH	6.2×10^{14}	7.8×10^{-10}
			CH_3CHO	5.1×10^{13}	6.4×10^{-11}
			CH_3OCHO	5.4×10^{13}	6.8×10^{-11}
			C_2H_5OH	1.0×10^{14}[a]	1.2×10^{-10}
			HCCCHO	2.6×10^{13}[a]	3.2×10^{-11}
			CH_3OCH_3	6.0×10^{13}[b]	7.6×10^{-11}
			CH_3CN	4.95×10^{12}[b]	6.3×10^{-12}
IRAS4A	0.5″ López-Sepulcre et al. 2015	2.5×10^{24} López-Sepulcre et al. 2015	CH_3OH (hot)	9.7×10^{16}	3.9×10^{-8}
			CH_3CHO	4.4×10^{15}	1.8×10^{-9}
			CH_3OCHO	2.4×10^{16}	9.5×10^{-9}
			C_2H_5OH	1.3×10^{16}	5.2×10^{-9}
			HCCCHO	4.9×10^{15}[a]	2.0×10^{-9}
			CH_3OCH_3	6.7×10^{15}	2.7×10^{-9}
			CH_3CN	3.55×10^{15}	1.4×10^{-09}
SVS13A	1″ López-Sepulcre et al. 2015	1.0×10^{25} López-Sepulcre et al. 2015	CH_3OH	3.7×10^{16}	3.7×10^{-9}
			CH_3CHO	8.6×10^{14}	8.6×10^{-11}
			CH_3OCHO	9.7×10^{15}	9.7×10^{-10}
			C_2H_5OH	2.8×10^{15}	2.8×10^{-10}
			HCCCHO	3.9×10^{16}[a]	3.9×10^{-9}
			CH_3OCH_3	1.3×10^{16}[c]	1.3×10^{-9}
			CH_3CN	5.16×10^{14}	5.2×10^{-11}
SVS13A	0.3″ Bianchi et al. 2019	3.0×10^{24} Chen et al. 2009	CH_3OH	4.1×10^{17}	1.4×10^{-7}
			CH_3CHO	9.6×10^{15}	3.2×10^{-9}
			CH_3OCHO	1.1×10^{17}	3.6×10^{-8}
			C_2H_5OH	3.1×10^{16}	1.0×10^{-8}
			HCCCHO	4.3×10^{17}[a]	1.4×10^{-7}
			CH_3OCH_3	1.4×10^{17}[d]	4.7×10^{-8}
			CH_3CN	5.74×10^{15}	1.9×10^{-09}

Notes.
[a] Indicates upper limit,
[b] indicates LTE-derived value,
[c] is scaled value from Bianchi et al. (2019), and
[d] from Bianchi et al. (2019),
[e] taken from Hily-Blant et al. (2022) after scaling it for 10″,
[f] taken from Daniel et al. (2013) after scaling it for 10″.

source size of 0.3″ for various iCOMs . We adopt both sizes to consider the beam dilution effect (see Table E1 and Figure E1).

Figure E1 depicts that even with the beam dilution effect, the obtained trend is similar (the abundance is gradually increasing up to class 0 and then decreased) to that obtained without the beam dilution effect shown in Figure 1. A very similar trend was also obtained when we used the abundances from various interferometric observations in Figure 6.

ORCID iDs

Bratati Bhat https://orcid.org/0000-0002-5224-3026
Rumela Kar https://orcid.org/0000-0002-5842-1356
Suman Kumar Mondal https://orcid.org/0000-0002-7657-1243
Rana Ghosh https://orcid.org/0000-0003-1745-9718
Prasanta Gorai https://orcid.org/0000-0003-1602-6849
Takashi Shimonishi https://orcid.org/0000-0002-0095-3624
Kei E. I. Tanaka https://orcid.org/0000-0002-6907-0926
Kenji Furuya https://orcid.org/0000-0002-2026-8157
Ankan Das https://orcid.org/0000-0003-4615-602X

References

Andre, P., Ward-Thompson, D., & Barsony, M. 1993, ApJ, 406, 122
Anglada, G., Rodríguez, L. F., & Torrelles, J. M. 2000, ApJL, 542, L123
Bachiller, R., Guilloteau, S., Gueth, F., et al. 1998, A&A, 339, L49
Balucani, N., Ceccarelli, C., & Taquet, V. 2015, MNRAS: Letters, 449, L16
Belloche, A., Maury, A. J., Maret, S., et al. 2020, A&A, 635, A198
Bhat, B., Gorai, P., Mondal, S. K., Chakrabarti, S. K., & Das, A. 2022, AdSpR, 69, 415
Bianchi, E., Ceccarelli, C., Codella, C., et al. 2022b, A&A, 662, A103
Bianchi, E., Codella, C., Ceccarelli, C., et al. 2019, MNRAS, 483, 1850
Bianchi, E., López-Sepulcre, A., Ceccarelli, C., et al. 2022a, ApJL, 928, L3
Bizzocchi, L., Caselli, P., Spezzano, S., & Leonardo, E. 2014, A&A, 569, A27

Blake, G. A., Sandell, G., van Dishoeck, E. F., et al. 1995, ApJ, 441, 689
Blake, G. A., Sutton, E., Masson, C., & Phillips, T. 1987, ApJ, 315, 621
Bockelée-Morvan, D., Lis, D. C., Wink, J. E., et al. 2000, A&A, 353, 1101
Bottinelli, S., Ceccarelli, C., Lefloch, B., et al. 2004, ApJ, 615, 354
Bottinelli, S., Ceccarelli, C., Williams, J. P., & Lefloch, B. 2007, A&A, 463, 601
Calcutt, H., Jørgensen, J. K., Müller, H. S. P., et al. 2018, A&A, 616, A90
Caselli, P., Bizzocchi, L., Keto, E., et al. 2017, A&A, 603, L1
Caselli, P., & Ceccarelli, C. 2012, A&ARv, 20, 56
Caselli, P., Pineda, J. E., Sipilä, O., et al. 2022, ApJ, 929, 13
Caselli, P., Pineda, J. E., Zhao, B., et al. 2019, ApJ, 874, 89
Caselli, P., Walmsley, C. M., Tafalla, M., Dore, L., & Myers, P. C. 1999, ApJL, 523, L165
Caselli, P., Walmsley, C. M., Zucconi, A., et al. 2002, ApJ, 565, 344
Cazaux, S., Tielens, A. G. G. M., Ceccarelli, C., et al. 2003, ApJL, 593, L51
Cernicharo, J., & Guelin, M. 1987, A&A, 176, 299
Cernicharo, J., Marcelino, N., Roueff, E., et al. 2012, ApJL, 759, L43
Cernicharo, J., Tercero, B., Fuente, A., et al. 2013, ApJL, 771, L10
Chen, X., Launhardt, R., & Henning, T. 2009, ApJ, 691, 1729
Choi, M., Kang, M., & Tatematsu, K. 2011, ApJL, 728, L34
Choi, M., Panis, J.-F., & Evans, N. J. I. 1999, ApJS, 122, 519
Choi, M., Tatematsu, K., & Kang, M. 2010, ApJL, 723, L34
Ciolek, G. E., & Basu, S. 2000, ApJ, 529, 925
Cuppen, H., Walsh, C., Lamberts, T., et al. 2017, SSRv, 212, 1
Daniel, F., Gérin, M., Roueff, E., et al. 2013, A&A, 560, A3
Das, A., Acharyya, K., Chakrabarti, S., & Chakrabarti, S. K. 2008, A&A, 486, 209
Das, A., Acharyya, K., & Chakrabarti, S. K. 2010, MNRAS, 409, 789
Das, A., & Chakrabarti, S. K. 2011, MNRAS, 418, 545
Das, A., Gorai, P., & Chakrabarti, S. K. 2019, A&A, 628, A73
Das, A., Sahu, D., Majumdar, L., & Chakrabarti, S. K. 2016, MNRAS, 455, 540
Das, A., Sil, M., Gorai, P., Chakrabarti, S. K., & Loison, J. C. 2018, ApJS, 237, 9
De Simone, M., Ceccarelli, C., Codella, C., et al. 2020, ApJL, 896, L3
Di Francesco, J., Myers, P. C., Wilner, D. J., Ohashi, N., & Mardones, D. 2001, ApJ, 562, 770
Diaz-Rodriguez, A. K., Anglada, G., Blázquez-Calero, G., et al. 2022, ApJ, 930, 91
Doty, S. D., Everett, S. E., Shirley, Y. L., Evans, N. J., & Palotti, M. L. 2005, MNRAS, 359, 228
Fuente, A., Cernicharo, J., Roueff, E., et al. 2016, A&A, 593, A94
Fuente, A., Gerin, M., Pety, J., et al. 2017, A&A, 606, L3
Galli, P. A. B., Loinard, L., Bouy, H., et al. 2019, A&A, 630, A137
Garrod, R. T., & Herbst, E. 2006, A&A, 457, 927
Garrod, R. T., Vasyunin, A. I., Semenov, D. A., Wiebe, D. S., & Henning, T. 2009, ApJL, 700, L43
Garrod, R. T., Wakelam, V., & Herbst, E. 2007, A&A, 467, 1103
Gerin, M., Marcelino, N., Biver, N., et al. 2009, A&A, 498, L9
Gerin, M., Pety, J., Fuente, A., et al. 2015, A&A, 577, L2
Ghosh, R., Sil, M., Kumar Mondal, S., et al. 2022, RAA, 22, 065021
Goldsmith, P. F., & Langer, W. D. 1999, ApJ, 517, 209
Gorai, P., Bhat, B., Sil, M., et al. 2020, ApJ, 895, 86
Gorai, P., Das, A., Shimonishi, T., et al. 2021, ApJ, 907, 108
Hasegawa, T. I., Herbst, E., & Leung, C. M. 1992, ApJS, 82, 167
Hily-Blant, P., Des Forêts, G. P., Faure, A., & Lique, F. 2022, A&A, 658, A168
Holdship, J., Viti, S., Codella, C., et al. 2019, ApJ, 880, 138
Huang, Y.-H., & Hirano, N. 2013, ApJ, 766, 131
Hudson, R. L., & Gerakines, P. A. 2019, MNRAS, 482, 4009
Irvine, W. M., Brown, R., Cragg, D., et al. 1988, ApJ, 335, L89
Jaber, A. A., Ceccarelli, C., Kahane, C., & Caux, E. 2014, ApJ, 791, 29
Jacobsen, S. K., Jørgensen, J. K., Di Francesco, J., et al. 2019, A&A, 629, A29
Jiménez-Serra, I., Vasyunin, A. I., Caselli, P., et al. 2016, ApJL, 830, L6
Johnson, D. G., Blitz, M. A., & Seakins, P. W. 2000, PCCP, 2, 2549
Johnstone, D., Rosolowsky, E., Tafalla, M., & Kirk, H. 2010, ApJ, 711, 655
Jørgensen, J. K., Hogerheijde, M. R., van Dishoeck, E. F., Blake, G. A., & Schöier, F. L. 2004, A&A, 413, 993
Jørgensen, J. K., Müller, H. S. P., Calcutt, H., et al. 2018, A&A, 620, A170
Jørgensen, J. K., van der Wiel, M. H. D., Coutens, A., et al. 2016, A&A, 595, A117
Keto, E., & Caselli, P. 2010, MNRAS, 402, 1625
Kuan, Y.-J., Huang, H.-C., Charnley, S. B., et al. 2004, ApJ, 616, L27
Lattanzi, V., Bizzocchi, L., Vasyunin, A. I., et al. 2020, A&A, 633, A118
Lefloch, B., Bachiller, R., Ceccarelli, C., et al. 2018, MNRAS, 477, 4792
Lefloch, B., Castets, A., Cernicharo, J., Langer, W. D., & Zylka, R. 1998, A&A, 334, 269
Loison, J.-C., Agúndez, M., Marcelino, N., et al. 2016, MNRAS, 456, 4101
Looney, L. W., Tobin, J. J., & Kwon, W. 2007, ApJL, 670, L131
López-Sepulcre, A., Jaber, A. A., Mendoza, E., et al. 2015, MNRAS, 449, 2438
López-Sepulcre, A., Sakai, N., Neri, R., et al. 2017, A&A, 606, A121
Mangum, J. G., & Wootten, A. 1993, ApJS, 89, 123
Marcelino, N., Agúndez, M., Cernicharo, J., Roueff, E., & Tafalla, M. 2018a, A&A, 612, L10
Marcelino, N., Cernicharo, J., Tercero, B., & Roueff, E. 2009, ApJL, 690, L27
Marcelino, N., Gerin, M., Cernicharo, J., et al. 2018b, A&A, 620, A80
Maret, S., Ceccarelli, C., Caux, E., Tielens, A. G. G. M., & Castets, A. 2002, A&A, 395, 573
Maret, S., Ceccarelli, C., Caux, E., Tielens, A. G. G. M., & Castets, A. 2002, A&A, 395, 573
Maret, S., Ceccarelli, C., Tielens, A. G. G. M., et al. 2005, A&A, 442, 527
Margulès, L., McGuire, B., Evans, C., et al. 2020, A&A, 642, A206
Marvel, K. B., Wilking, B. A., Claussen, M. J., & Wootten, A. 2008, ApJ, 685, 285
Mondal, S. K., Gorai, P., Sil, M., et al. 2021, ApJ, 922, 194
Mondal, S. K., Iqbal, W., Gorai, P., et al. 2023, A&A, 669, A71
Müller, H. S. P., Schlöder, F., Stutzki, J., & Winnewisser, G. 2005, JMoSt, 742, 215
Müller, H. S. P., Thorwirth, S., Roth, D. A., & Winnewisser, G. 2001, A&A, 370, L49
Myers, P. C., Adams, F. C., Chen, H., & Schaff, E. 1998, ApJ, 492, 703
Nagy, Z., Spezzano, S., Caselli, P., et al. 2019, A&A, 630, A136
Nummelin, A., Bergman, P., Hjalmarson, Å., et al. 2000, ApJS, 128, 213
Öberg, K. I., Bottinelli, S., Jørgensen, J. K., & van Dishoeck, E. F. 2010, ApJ, 716, 825
Öberg, K. I., Bottinelli, S., & van Dishoeck, E. F. 2009, A&A, 494, L13
Ortiz-León, G. N., Loinard, L., Dzib, S. A., et al. 2018, ApJ, 865, 73
Peeters, Z., Rodgers, S., Charnley, S., et al. 2006, A&A, 445, 197
Pezzuto, S., Elia, D., Schisano, E., et al. 2012, A&A, 547, A54
Pickett, H. M., Poynter, R. L., Cohen, E. A., et al. 1998, JQSRT, 60, 883
Redaelli, E., Bizzocchi, L., Caselli, P., et al. 2019, A&A, 629, A15
Reipurth, B., Chini, R., Krugel, E., Kreysa, E., & Sievers, A. 1993, A&A, 273, 221
Sahu, D., Liu, S.-Y., Su, Y.-N., et al. 2019, ApJ, 872, 196
Sahu, D., Minh, Y. C., Lee, C.-F., et al. 2018, MNRAS, 475, 5322
Santangelo, G., Codella, C., Cabrit, S., et al. 2015, A&A, 584, A126
Schlafly, E. F., Green, G., Finkbeiner, D. P., et al. 2014, ApJ, 786, 29
Scibelli, S., & Shirley, Y. 2020, ApJ, 891, 73
Shimonishi, T., Onaka, T., Kawamura, A., & Aikawa, Y. 2016, ApJ, 827, 72
Sil, M., Srivastav, S., Bhat, B., et al. 2021, AJ, 162, 119
Snyder, L., Buhl, D., Schwartz, P., et al. 1974, ApJ, 191, L79
Srivastav, S., Sil, M., Gorai, P., et al. 2022, MNRAS, 515, 3524
Sutton, E., Peng, R., Danchi, W., et al. 1995, ApJS, 97, 455
Tafalla, M., Mardones, D., Myers, P. C., et al. 1998, ApJ, 504, 900
Taquet, V., López-Sepulcre, A., Ceccarelli, C., et al. 2015, ApJ, 804, 81
Turner, B. E., Terzieva, R., & Herbst, E. 1999, ApJ, 518, 699
Vastel, C., Ceccarelli, C., Lefloch, B., & Bachiller, R. 2014, ApJL, 795, L2
Vastel, C., Quénard, D., Le Gal, R., et al. 2018, MNRAS, 478, 5514
Vasyunin, A. I., Caselli, P., Dulieu, F., & Jiménez-Serra, I. 2017, ApJ, 842, 33
Wakelam, V., Loison, J. C., Mereau, R., & Ruaud, M. 2017, MolAs, 6, 22
Yang, Y.-L., Sakai, N., Zhang, Y., et al. 2021, ApJ, 910, 20
Zucker, C., Schlafly, E. F., Speagle, J. S., et al. 2018, ApJ, 869, 83
Zuckerman, B., Turner, B., Johnson, D., et al. 1975, ApJ, 196, L99